Norwegian Sea net community production estimated from O_2 and prototype CO_2 optode measurements on a Seaglider

Luca Possenti[1], Ingunn Skjelvan[2], Dariia Atamanchuk[3], Anders Tengberg[4], Matthew P. Humphreys[5], Socratis Loucaides[6], Liam Fernand[7], Jan Kaiser[1]

[1]Centre for Ocean and Atmospheric Sciences, School of Environmental Sciences, University of East Anglia, Norwich, UK

[2]NORCE Norwegian Research Centre, Bjerknes Centre for Climate Research, Bergen, Norway

[3]Dalhousie University, Halifax, Canada

[4]University of Gothenburg, Sweden

[5]NIOZ Royal Netherlands Institute for Sea Research, Department of Ocean Systems (OCS), and Utrecht University, Texel, the Netherlands

[6]National Oceanography Centre, European Way, Southampton, SO14 3ZH, UK

[7]Centre for Environment, Fisheries and Aquaculture Sciences, Lowestoft, UK, NR33 0HT

Correspondence to: Luca Possenti (L.Possenti@uea.ac.uk)

Abstract. We report on a pilot study using a CO_2 optode deployed on a Seaglider in the Norwegian Sea for 8 months (March to October 2014). The optode measurements required drift- and lag-correction, and in situ calibration using discrete water samples collected in the vicinity. We found the optode signal correlated better with the concentration of CO_2, $c(CO_2)$, than with its partial pressure, $p(CO_2)$. Using the calibrated $c(CO_2)$ and a regional parameterisation of total alkalinity (A_T) as a function of temperature and salinity, we calculated total dissolved inorganic carbon concentrations, C_T, which had a standard deviation of 10 μmol kg^{-1} compared with direct C_T measurements. The glider was also equipped with an oxygen (O_2) optode. The O_2 optode was drift-corrected and calibrated using a $c(O_2)$ climatology for deep samples (R^2 = 0.89; RMSE = 0.009 μmol kg^{-1}). The calibrated data enabled the calculation of C_T- and $c(O_2)$-based net community production, $N(C_T)$ and $N(O_2)$. To derive N, C_T and O_2 inventory changes over time were combined with estimates of air-sea gas exchange, diapycnal mixing and entrainment of deeper waters. Glider-based observations captured two periods of increased Chl *a* inventory in late spring (May) and a second one in summer (June). For the May period, we found $N(C_T)$ = (23±4.2) mmol m^{-2} d^{-1}, $N(O_2)$ = (94±24) mmol m^{-2} d^{-1} and an (uncalibrated) Chl *a* peak concentration of c_{raw}(Chl *a*) = 3 mg m^{-3}. During the June period, c_{raw}(Chl *a*) increased to a summer maximum of 4 mg m^{-3}, associated with $N(C_T)$ = (14±8.7) mmol m^{-2} d^{-1} and $N(O_2)$ = (126±25) mmol m^{-2} d^{-1}. The high-resolution dataset allowed for quantification of the changes in N before, during and after the periods of increased Chl *a* inventory. After the May period, the remineralisation of the material produced during the period of increased Chl *a* inventory decreased $N(C_T)$ to (-4.5±5.2) mmol m^{-2} d^{-1} and $N(O_2)$ to (0±1.6) mmol m^{-2} d^{-1}. The survey area was a source of O_2 and a sink of CO_2 for most of the summer. The deployment captured two different surface waters: the

Norwegian Atlantic Current (NwAC) and the Norwegian Coastal Current (NCC). The NCC was characterised by lower $c(O_2)$ and C_T than the NwAC, as well as lower $N(O_2)$, $N(C_T)$ and c_{raw}(Chl *a*). Our results show the potential of glider data to simultaneously capture time and depth-resolved variability in C_T and O_2.

1 Introduction

Climate models project an increase in the atmospheric CO_2 mole fraction driven by anthropogenic emissions from a preindustrial value of 280 µmol mol^{-1} (Neftel et al., 1982) to 538-936 µmol mol^{-1} by 2100 (Pachauri and Reisinger, 2007). The ocean is known to be a major CO_2 sink (Sabine et al., 2004; Le Quéré et al., 2009; Sutton et al., 2014); in fact, it has taken up approximately 25 % of this anthropogenic CO_2 with a rate of (2.5±0.6) Gt a^{-1} (in C equivalents) (Friedlingstein et al., 2019). This uptake alters the carbonate system of seawater and is causing a decrease in seawater pH, a process known as ocean acidification (Gattuso and Hansson, 2011). The processes affecting the marine carbonate system include air-sea gas exchange, photosynthesis and respiration, advection and vertical mixing, and $CaCO_3$ formation and dissolution. For that reason, it is important to develop precise, accurate and cost-effective tools to observe CO_2 variability and related processes in the ocean. Provided that suitable sensors are available, autonomous ocean glider measurements may help resolve these processes.

To quantify the marine carbonate system, four variables are commonly measured: total dissolved inorganic carbon concentration (C_T), pH, total alkalinity (A_T) and the fugacity of CO_2 ($f(CO_2)$). At thermodynamic equilibrium, knowledge of two of the four variables is sufficient to calculate the other two. Marine carbonate system variables are primarily measured on research ships, commercial ships of opportunity, moorings, buoys and floats (Hardman-Mountford et al., 2008; Monteiro et al., 2009; Takahashi et al., 2009; Olsen et al., 2016; Bushinsky et al., 2019). Moorings equipped with submersible sensors often provide limited vertical and horizontal, but good long-term temporal resolution (Hemsley, 2015). In contrast, ship-based surveys have higher vertical and spatial resolution than moorings but limited repetition frequency because of the expense of ship operations. Ocean gliders have the potential to replace some ship surveys because they are much cheaper to operate and will increase our coastal and regional observational capacity. However, the slow glider speed of 1-2 km h^{-1} only allows a smaller spatial coverage than ship surveys and the sensors require careful calibration to match the quality of data provided by ship-based sampling.

Carbonate system sensors suitable for autonomous deployment have been developed in the past decades, in particular pH sensors (Martz et al., 2010; Rérolle et al., 2013; Seidel et al., 2008) and $p(CO_2)$ sensors (Goyet et al., 1992; Degrandpre, 1993; Körtzinger et al., 1996; Bittig et al., 2012; Atamanchuk, 2013). One of these sensors is the CO_2 optode (Atamanchuk et al., 2014) which has been successfully deployed to monitor an

artificial CO_2 leak on the Scottish west coast (Atamanchuk, et al., 2015b), on a cabled underwater observatory (Atamanchuk, et al., 2015a), to measure lake metabolism (Peeters et al., 2016), for fish transportation (Thomas et al., 2017) and on a moored profiler (Chu et al., 2020).

C_T and $c(O_2)$ can be used to calculate net community production (N), which is defined as the difference between gross primary production (G) and community respiration (R). At steady-state, N is equal to the rate of organic carbon export and transfer from the surface into the mesopelagic and deep waters (Lockwood et al., 2012). N is derived by vertical integration to a specific depth, that is commonly defined relative to the mixed layer depth (z_{mix}) or the bottom of the euphotic zone (Plant et al., 2016). A system is defined as autotrophic when G is larger than R (i.e. N is positive) and as heterotrophic when R is larger than G (i.e. N is negative) (Ducklow and Doney, 2013).

N can be quantified using bottle incubations or in situ biogeochemical budgets (Sharples et al., 2006; Quay, et al, 2012; Seguro et al., 2019). Bottle incubations involve measuring production and respiration in vitro under dark and light conditions. Biogeochemical budgets combine O_2 and C_T inventory changes with estimates of air-sea gas exchange, entrainment, advection and vertical mixing (Alkire et al., 2014; Binetti et al., 2020; Neuer et al., 2007).

The Norwegian Sea is a complex environment due to the interaction between the Atlantic Water (NwAC) entering from the south-west, Arctic Water coming from the north and the Norwegian Coastal Current (NCC) flowing along the Norwegian coast (Nilsen and Falck, 2006). In particular, Atlantic Water enters the Norwegian Sea through the Faroe-Shetland Channel and Iceland-Faroe Ridge (Hansen and Østerhus, 2000) with salinity S between 35.1 and 35.3 and temperatures warmer than 6 ˚C (Swift, 1986). The NCC water differs from the NwAC with a surface $S < 35$ (Saetre and Ljoen, 1972) and a seasonal θ signal (Nilsen and Falck, 2006).

Biological production in the Norwegian Sea varies during the year and can be divided into 5 periods (Rey, 2001): (1) winter with the smallest productivity and phytoplankton biomass; (2) a pre-bloom period; (3) the spring bloom when productivity increases and phytoplankton biomass reaches the annual maximum; (4) a post-bloom period with productivity mostly based on regenerated nutrients; (5) autumn with smaller blooms than in summer. Previous estimates of $N(C_T)$ were based on discrete C_T samples (Falck and Anderson, 2005) or were calculated from $c(O_2)$ measurements and converted to C equivalents assuming Redfield stoichiometry of production/respiration (Falck and Gade, 1999; Kivimäe, 2007; Skjelvan et al., 2001). Glider measurements have been used to estimate N in other ocean regions (Nicholson et al., 2008; Alkire et al., 2014; Haskell et al., 2019; Binetti et al., 2020); however, as far as we know, this is the first study of net community production in the

Norwegian Sea using a high-resolution glider dataset (>10^6 data points; 40 s time resolution) and the first anywhere estimating *N* from a glider-mounted sensor directly measuring the marine carbonate system.

2 Material and methods

2.1 Glider sampling

Kongsberg Seaglider 564 was deployed in the Norwegian Sea on 16 March 2014 at 63.00° N, 3.86° E and recovered on 30 October 2014 at 62.99° N, 3.89° E. The Seaglider was equipped with a prototype Aanderaa 4797 CO_2 optode, an Aanderaa 4330F oxygen optode (Tengberg et al., 2006), a Seabird CTD and a combined backscatter/chlorophyll *a* fluorescence sensor (Wetlabs Eco Puck BB2FLVMT). The mean sampling intervals for each sensor varied with depth (Table 1). On average in the top 100 m the CTD performed an in situ measurement every 24 s, the O_2 optode every 49 s, the CO_2 optode every 106 s and the fluorescence sensor every 62 s. The sampling interval increased in depths between 100 to 500 m to 31 s for the CTD, 153 s for the O_2 optode and 233 s for the CO_2 optode. The sampling interval reached its maximum at depths between 500 to 1000 m where was 42 s for the CTD, 378 s for the O_2 optode and 381 d for the CO_2 optode.

Table 1. Average sampling interval of Seabird CTD, Aanderaa 4330F oxygen optode, Aanderaa 4797 CO_2 optode and a combined backscatter/chlorophyll *a* fluorescence sensor (Wetlabs Eco Puck BB2FLVMT) in the top 100 m, from 100 to 500 and from 500 to 1000 m.

Depth / m	*t*(CTD) / s	*t*(O_2) / s	*t*(CO_2) / s	*t*(Chl *a*) / s
0 – 100 m	24	49	106	62
100 – 500 m	31	153	233	-
500 – 1000 m	42	378	381	-

The deployment followed the Svinøy trench, from the open sea towards the Norwegian coast. The glider covered a 536 km long transect 8 times (4 times in each direction) for a total of 703 dives (Figure 1).

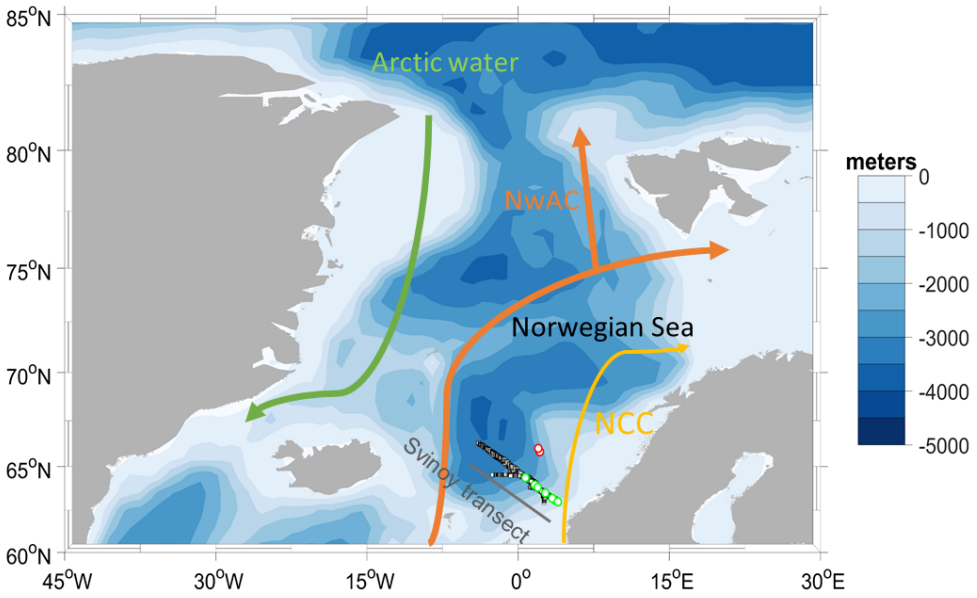

Figure 1: Map of the glider deployment and the main water masses. The black dots are the glider dives, the green and the red dots are the water samples collected along the glider section and at OWSM, respectively. The three main water masses (Skjelvan et al., 2008) are the Norwegian Coastal Current (yellow), the Norwegian Atlantic Current (NwAC, orange) and Arctic Water (green).

2.2 Discrete sampling

During the glider deployment, 70 discrete water samples from various depths (5, 10, 20, 30, 50, 100, 300, 500 and 1000 m) were collected on 4 different cruises on the R/V Haakon Mosby along the southern half of the glider transect on 18 March, 5 May, 6 and 14 June, and 30 October 2014. Samples for C_T and A_T were collected from 10 L Niskin bottles following the standard operational procedure (SOP) 1 of Dickson et al. (2007). The C_T and A_T samples were preserved with saturated $HgCl_2$ solution (final $HgCl_2$ concentration: 15 mg dm^{-3}). Nutrient samples from the same Niskin bottles were preserved with chloroform (Hagebo and Rey, 1984). C_T and A_T were analysed on shore according to SOP 2 and 3b (Dickson et al., 2007) using a VINDTA 3D (Marianda) with a CM5011 coulometer (UIC instruments) and a VINDTA 3S (Marianda), respectively. Nutrients were analysed on shore using an Alpkem Auto Analyzer. In addition, 43 water samples were collected at Ocean Weather Station M (OWSM) on 5 different cruises on 22 March on R/V Haakon Mosby, on 9 May on R/V G.O. Sars, on 14 June on R/V Haakon Mosby, on 2 August and on 13 November 2014 on R/V Johan Hjort from 10, 30, 50, 100, 200, 500, 800 and 1000 m depth. The OWSM samples were preserved and analysed for A_T and C_T as the Svinøy samples. No phosphate and silicate samples were collected at OSWM. Temperature (θ) and salinity (S) profiles were measured at each station using a SeaBird 911 plus CTD. pH and $f(CO_2)$ were calculated using the MATLAB toolbox CO2SYS (Van Heuven et al., 2011), with the following constants: K_1 and K_2 carbonic acid dissociation constants of Lueker et al. (2000), $K(HSO_4^-/SO_4^{2-})$ bisulfate dissociation constant of Dickson (1990)

and borate to chlorinity ratio of Lee et al. (2010). In the OWSM calculations, we used nutrient concentrations from the Svinøy section at a time as close as possible to the OWSM sampling as input. In the case of the glider, we derived a parameterisation for phosphate and silicate concentration as a function of sample depth and time. This parameterisation had an uncertainty of 1.3 and 0.13 μmol kg^{-1} and a R^2 of 0.6 and 0.4, for silicate and phosphate concentrations, respectively. The uncertainty was calculated as the root mean square difference between measured and parameterised concentrations. This nutrient concentration uncertainty contributed an uncertainty of 0.04 μmol kg^{-1} in the calculation of $c(CO_2)$, which is negligible.

2.3 Oxygen optode calibration

The last oxygen optode calibration before the deployment was performed in 2012 as a two-point calibration at 9.91 °C in air-saturated water and at 20.37 °C in anoxic Na_2SO_3 solution. Oxygen optodes are known to be affected by drift (Bittig et al., 2015), which is worse for the fast-response foils used in the 4330F optode for glider deployments. It has been suggested to calibrate and drift correct the optode using discrete samples or in-air measurements (Nicholson and Feen, 2017). Unfortunately, no discrete samples were collected at glider deployment or recovery.

To overcome this problem, we used archived data to correct for oxygen optode drift. These archived concentration data (designated $c_C(O_2)$) were collected at OWSM between 2001 and 2007 (downloaded from ICES data base) and in the glider deployment region between 2000 and 2018 (extracted from GLODAPv2; Olsen et al., 2016). To apply the correction, we used the oxygen samples corresponding to a potential density σ_0 > 1028 kg m^{-3} (corresponding to depths between 427 and 1000 m), because waters of these potential densities were always well below the mixed layer and therefore subject to limited seasonal and interannual variability, as evidenced by the salinity S and potential temperature θ of these samples: S varied from 34.88 to 34.96, with a mean of 34.90±0.01; θ varied from 0.45 to –0.76 °C, with a mean of (–0.15±0.36) °C.

Figure 2 shows that the glider oxygen concentration ($c_G(O_2)$) corresponding to σ_0 > 1028 kg m^{-3} was characterised by two different water masses separated at a latitude of about 64° N. We used the samples collected north of 64° N to derive the glider optode correction because this reflects the largest area covered by the glider. We did not use the southern region because the archived samples from there covered only 5 days. For each day of the year with archived samples, we calculated the median concentration of the glider and the archived samples. Figure 3 shows a plot of the ratio between $c_C(O_2)/c_G(O_2)$ against the day of the year and a linear fit, which is used to calibrate $c_G(O_2)$ and correct for drift.

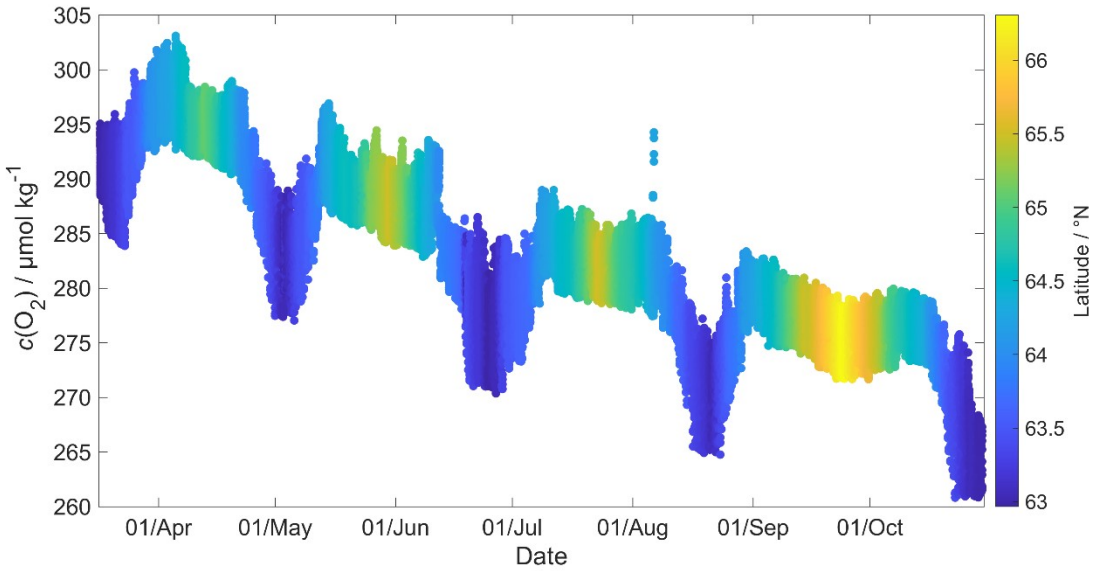

Figure 2: Glider oxygen concentration, $c_G(O_2)$, for $\sigma_0 > 1028$ kg m^{-3} coloured by latitude.

No lag correction was applied because the O_2 optode had a fast response foil and showed no detectable lag (<10 s), based on a comparison between descent and ascent profiles.

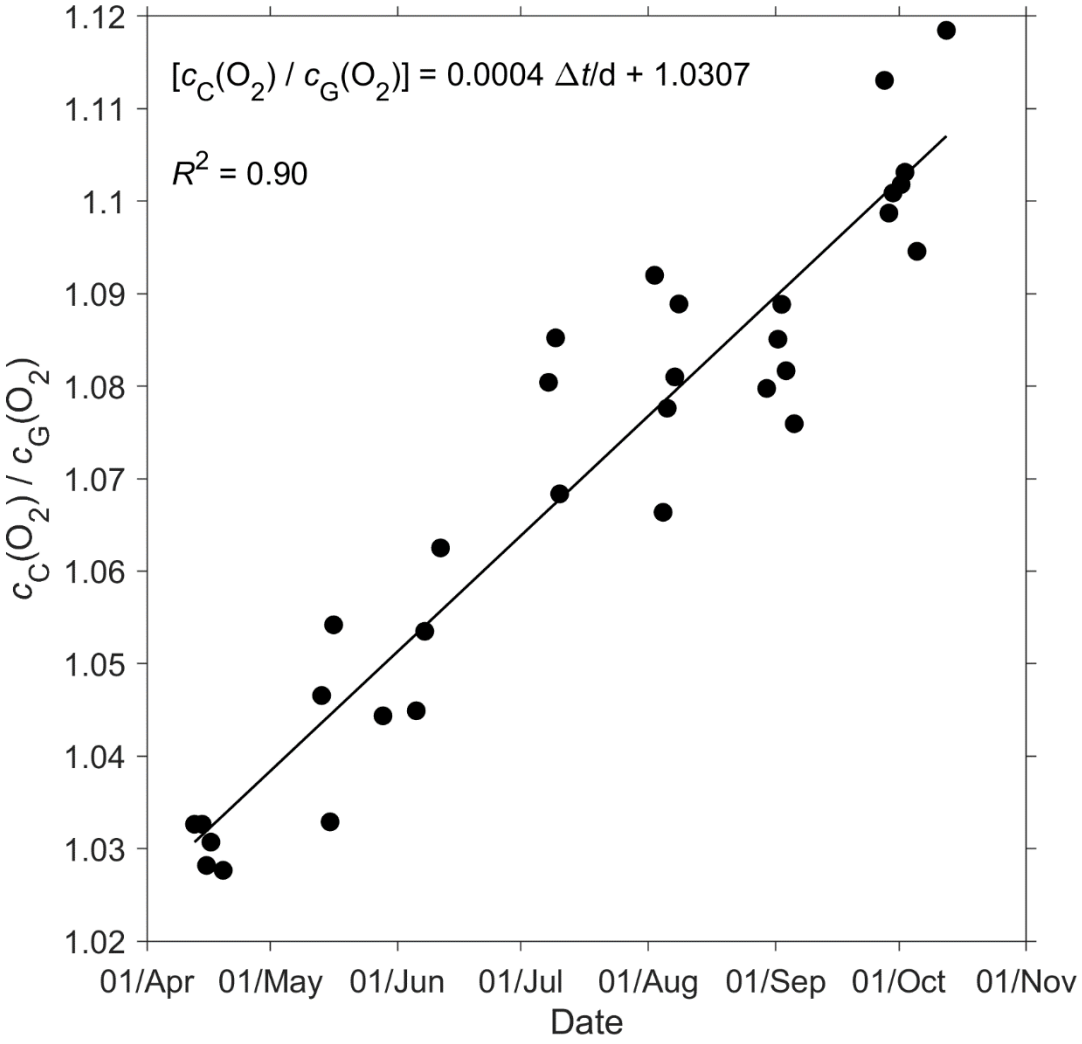

Figure 3:. The linear fit of the ratio between the daily median of the discrete oxygen samples ($c_C(O_2)$) and glider oxygen data ($c_G(O_2)$) for $\sigma_0 > 1028$ kg m^{-3} was used to derive the $c_G(O_2)$ drift and initial offset at deployment. The time difference Δt is calculated with respect to the deployment day of the 16th of March.

2.4 CO_2 optode measurement principle

The CO_2 optode consists of an optical and a temperature sensor incorporated into a pressure housing. The optical sensor has a sensing foil comprising two fluorescence indicators (luminophores), one of which is sensitive to pH changes and the other is not and thus used as a reference. The excitation and emission spectra of the two fluorescence indicators overlap, but the reference indicator has a longer fluorescence lifetime than the pH indicator. These two fluorescence lifetimes are combined using an approach known as Dual Lifetime Referencing (DLR) (Klimant et al., 2001; von Bültzingslöwen et al., 2002). From the phase shift (φ), the partial pressure of CO_2, $p(CO_2)$, is parameterised as an eight-degree polynomial (Atamanchuk et al., 2014):

$$\log [p(CO_2)/\mu atm] = C_0 + C_1 \varphi + \ldots + C_8 \varphi^8 \quad (1)$$

where C_0 to C_8 are temperature-dependent coefficients.

The partial pressure of CO_2 is linked to the CO_2 concentration, $c(CO_2)$, and the fugacity of CO2, $f(CO_2)$, via the following relationship:

$$c(CO_2) = p(CO_2) / [1 - p(H_2O) / p]\ F(CO_2) = K_0(CO_2)\ f(CO_2) \quad (2)$$

where $F(CO_2)$ is the solubility function (Weiss and Price, 1980), $p(H_2O)$ is the water vapour pressure, p is the total gas tension (assumed to be near 1 atm) and $K_0(CO_2)$ is the solubility coefficient. F and K_0 vary according to temperature and salinity.

2.5 CO_2 optode lag and drift correction and calibration

The CO_2 optode was fully functional between dives 31 (on 21 March 2014) and 400 (on 24 July 2014). After dive 400, the CO_2 optode stopped sampling in the top 150 m. Figure 4 shows the outcome of each calibration step described in this section (steps 1 and 2) and section 2.6 (step 3): 0) uncalibrated optode output (blue dots), 1) drift correction (red dots), 2) lag correction (green dots) and 3) calibration using discrete water samples (black dots).

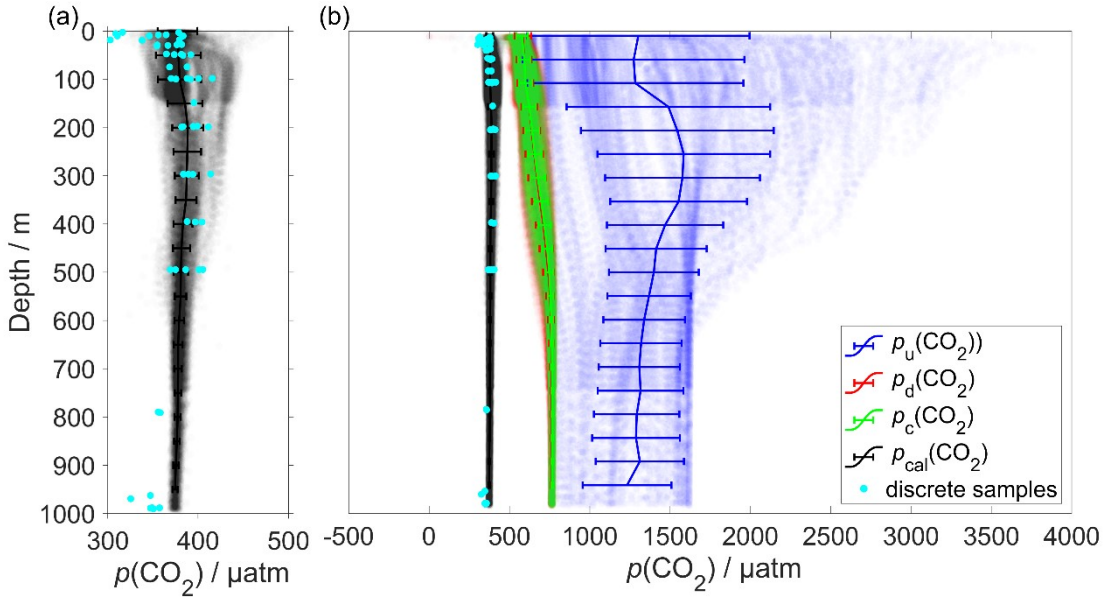

Figure 4: Panel a) shows in black the calibrated $p(CO_2)$ ($p_{cal}(CO_2)$) and in azure the discrete samples. b) Plot of $p(CO_2)$ versus depth where the vertical continuous lines are the mean every 50 m and the error bars represent the standard deviation. Blue colour shows $p_u(CO_2)$ without any correction; red shows $p_d(CO_2)$ corrected for drift, green represents $p_c(CO_2)$ corrected for drift and lag; black shows $p_{cal}(CO_2)$ calibrated against water samples (azure dots) collected during the deployment (section 2.6). $p_{cal}(CO_2)$ had a mean standard deviation of 22 µatm and a mean bias of 8.4 µatm compared with the discrete samples.

In order to correct for the drift occurring during the glider mission, we selected the CO_2 optode measurements in water with $\sigma_0 > 1028$ kg m^{-3} (just as for O_2; section 2.3). We calculated the median of the raw optode phase shift

data ("CalPhase" φ_{cal}) for each Seaglider dive. Then, we calculated a drift coefficient (m_i) as the ratio between the median φ_{cal} for a given dive divided by the median φ_{cal} of dive 31. Drift-corrected $\varphi_{cal,d}$ values were calculated by dividing the raw φ_{cal} by the specific m_i for each dive.

The CO_2 optode was also affected by lag (Atamanchuk et al., 2014) caused by the slow response of the optode to ambient $c(CO_2)$ changes in time and depth. The lag created a discrepancy between the depth profiles obtained during glider ascents and descents. To correct for this lag we applied the method of Miloshevich et al. (2004), which was previously used by Fiedler et al. (2013) and Atamanchuk et al. (2015b) to correct the lag of the Contros HydroC CO_2 sensor (Fiedler et al., 2013; Saderne et al., 2013). This CO_2 sensor has a different measurement principle (infrared absorption) than the CO_2 optode, but both rely on the diffusion of CO_2 through a gas-permeable membrane.

To apply the lag correction, the sampling interval (Δt) needs to be sufficiently small compared to the sensor response time (τ) and the ambient variability (Miloshevich, 2004). Before the lag correction, $\varphi_{cal,d}$ was rLOWESS-smoothed to remove any outliers and "kinks" in the profile. The smoothing function applies a local regression every 9 points using a weighted robust linear least-squares fit. Subsequently, τ was determined such that the following lag-correction equation (Miloshevich, 2004) minimised the $\varphi_{cal,d}$ difference between each glider ascent and the following descent:

$$p_c(CO_2, t_1) = \frac{p_d(CO_2,t_1) - p_d(CO_2,t_0)\ e^{-\Delta t/\tau}}{1 - e^{-\Delta t/\tau}} \quad (3)$$

where $p_d(CO_2,t_0)$ is the drift-corrected value measured by the optode at time t_0, $p_d(CO_2,t_1)$ is the measured value at time t_1, Δt is the time between t_0 and t_1, τ is the response time, and $p_c(CO_2,t_1)$ is the lag-corrected value at t_1. We calculated a τ value for each glider dive and used the median of τ (1384 s, 25th quartile: 1101 s; 75th quartile: 1799 s) (Figure 5), which was larger than Δt (258 s) and therefore met the requirement to apply the Miloshevich (2004) method. To apply the lag correction the glider needs to sample same water mass during the ascent and descent. The difference between the ascent and descent was minimal because was (0.13±0.33) ºC for θ and 0.02±0.04 for S. This lag correction reduced the average difference between the glider ascent and descent from (71±30) µatm to (21±26) µatm.

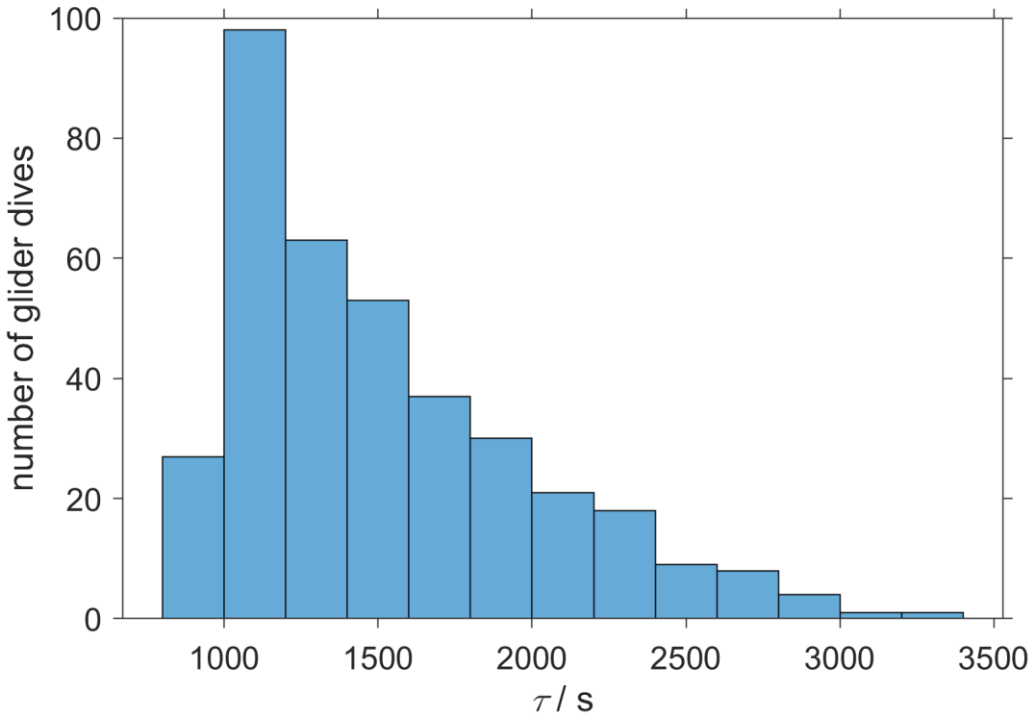

Figure 5: The histogram shows the distribution of the τ calculated from glider dive 31 to 400 to correct the CO_2 optode drift using the algorithm of Miloshevich (2004).

The CO_2 optode output was calibrated using the discrete samples collected throughout the mission. Using the discrete sample time and potential density σ_0, we selected the closest CO_2 optode output. Figure 6 shows a linear regression between optode output and $c(CO_2)$ from the discrete samples ($c_{WS}(CO_2)$), which was used to calibrate the optode output $p_c(CO_2)$ in terms of $c(CO_2)$. We used $c(CO_2)$ because it had a better correlation than $p(CO_2)$ ($R^2 = 0.77$ vs. $R^2 = 0.02$). The residual difference in $c(CO_2)$ between glider and water samples had a standard deviation of 1.3 µmol kg^{-1}.

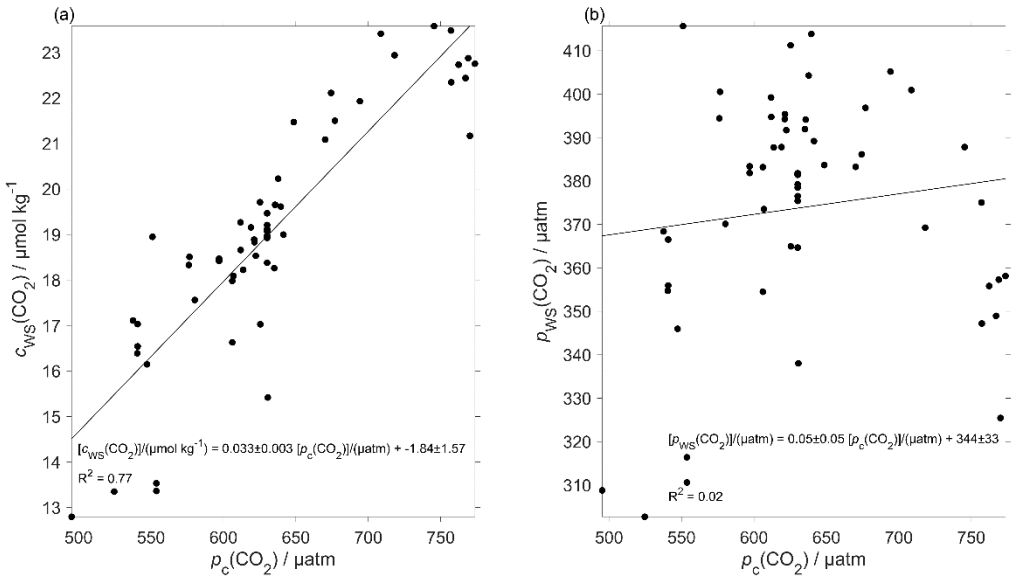

Figure 6: Calibration of the CO_2 optode using a) CO_2 concentration of the discrete samples ($c_{WS}(CO_2)$) against the glider output with the linear regression line and b) CO_2 partial pressure of the discrete samples ($p_{WS}(CO_2)$) against the glider output with the linear regression line.

2.6 Regional algorithm to estimate A_T

To calculate C_T, we used two variables: glider $c(CO_2)$ derived as described in section 2.6 and A_T derived using a regional algorithm based on S and θ in the top 1000 m. The algorithm followed the approach of Lee et al. (2006) and was derived using 663 water samples collected at OWSM from 2004 to 2014 and GLODAPv2 (Olsen et al., 2016) data from 2000 in the deployment region. Discrete samples with $S < 33$ were removed because these values were lower than the minimum S measured by the glider. The derived A_T parameterisation is:

$$A_{T,reg}/(\mu mol\ kg^{-1}) = 2317.03 + 33.12\ (S–35) + 7.94\ (S–35)^2 + 0.96\ (\theta/°C–20) + 0.01\ (\theta/°C–20)^2 \quad (4)$$

The parameterisation has an uncertainty of 8.2 µmol kg^{-1} calculated as the standard deviation of the residual difference between actual and parameterised A_T.

To test this parameterisation, we compared the predicted $A_{T,reg}$ values with discrete measurements ($A_{T,WS}$) collected close in terms of time, potential density (σ_0) and distance to the glider transect ($n = 60$). These discrete samples and the glider had mean temperature and salinity differences of (0.17±0.68) °C and 0.03±0.013, respectively. The mean difference between $A_{T,WS}$ and $A_{T,reg}$ was (2.1±6.5) µmol kg^{-1}.

This A_T parameterisation was used in CO2SYS (Van Heuven et al., 2011) to calculate C_T from $A_{T,reg}$ and the calibrated $c(CO_2)$, $c_{G,cal}(CO_2)$. These calculated $C_{T,cal}$ values were compared with $C_{T,WS}$ of the same set of discrete samples used to calibrate $c_{G,cal}(CO_2)$, the only difference being that instead of the actual total alkalinity of the water sample ($A_{T,WS}$), we used $A_{T,reg}$. The mean difference between $C_{T,cal}$ and $C_{T,reg}$ was (1.5±10) µmol kg^{-}

271 [1], with the non-zero bias and the standard deviation due to the uncertainties in the A_{Treg} parameterisation and the
272 $c_{G,cal}(CO_2)$ calibration.

273 **2.7 Quality control of other measurement variables**

274 The thermal lag of the glider conductivity sensor was corrected using the method of Gourcuff (2014). Single-
275 point outliers in conductivity were removed and replaced by linear interpolation. The glider CTD salinity was
276 affected by presumed particulate matter stuck in the conductivity cell (Medeot et al., 2011) during dives 147,
277 234, 244, 251, 272, 279, 303, 320 and 397 and sensor malfunction caused a poor match between glider ascent
278 and descent during a dives 214, 215, 235 and 243. These dives were removed from the subsequent analysis.

279 Glider-reported chlorophyll concentrations, c_{raw}(Chl *a*), were computed using the factory coefficients. c_{raw}(Chl *a*)
280 was affected by photochemical quenching during the daytime dives. To correct for quenching, we used the
281 method of Hemsley et al. (2015) based on the night-time relationship between fluorescence and optical
282 backscatter. This relationship was established in the top 60 meters and the night-time values were selected
283 between sunset and sunrise. We calculated a linear fit between c_{raw}(Chl *a*) measured at night, c_N(Chl *a*), and the
284 backscatter signal measured at night (b_N). The slope and the intercept were then used to derive corrected daytime
285 c_D(Chl *a*). The glider-reported chlorophyll concentration has not been calibrated against in situ samples and is
286 not expected to be accurate, even after correction for quenching. However, it should give an indication of the
287 depth of the deep chlorophyll concentration maximum (z_{DCM}) and the direction of chlorophyll concentration
288 change (up/down). 8 day-means of c_{raw}(Chl *a*) were compared with satellite 8 day-composite chlorophyll
289 concentration (Figure 7) from Ocean Colour CCI (https://esa-oceancolour-cci.org/) and gave a mean
290 difference of (0.12±0.08) mg m^{-3}.

291

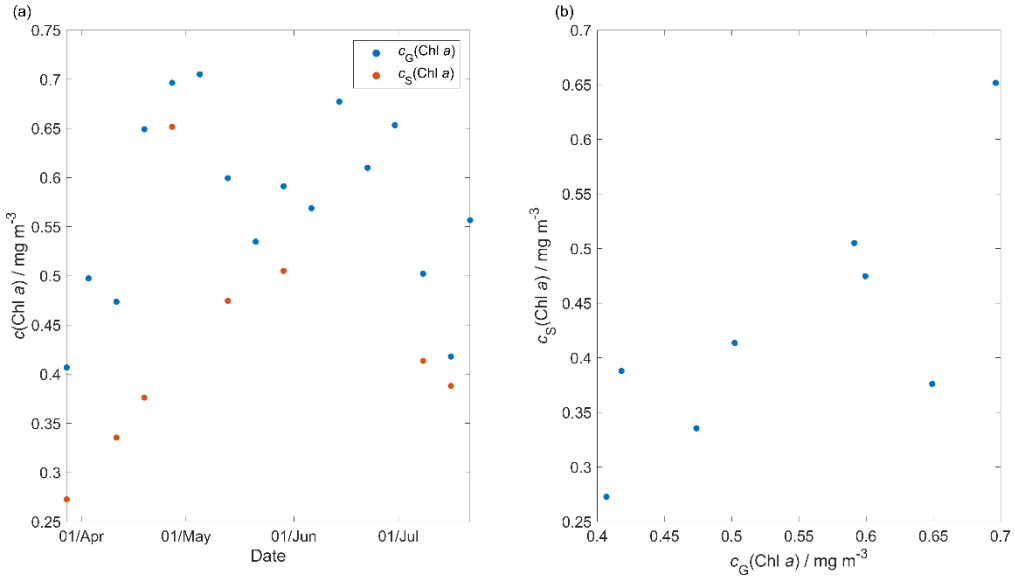

Figure 7: Comparison between the 8 day-glider *c*(Chl *a*) (c_G(Chl *a*)) mean and the 8 day-satellite *c*(Chl *a*) (c_S(Chl *a*)) download from Ocean Colour CCI (https://esa-oceancolour-cci.org/), as time-series (panel a) and scatter plot (panel b).

2.8 Calculation of oxygen-based net community production $N(O_2)$

Calculating net community production N from glider data is challenging because the glider continuously moves through different water masses. For that reason we subdivided the transect by binning the data into 0.1° latitude intervals to derive O_2 concentration changes every two transects. The changes were calculated between transects in the same direction of glider travel (e.g. transects 1 and 3, both in N-S direction) to have approximately the same time difference (40-58 days) at every latitude. If instead we had used two consecutive transects, this would lead to a highly variable time difference of near-0 to about 50 days along the transect.

We calculated $N(O_2)$ (in mmol m^{-2} d^{-1}) from the oxygen inventory changes ($I(O_2)$) corrected for air-sea exchange $\Phi(O_2)$, normalised to z_{mix} when z_{mix} was deeper than the integration depth of z_{lim} = 45 m, entrainment $E(O_2)$ and diapycnal eddy diffusion $F_v(O_2)$:

$$N(O_2) = I(O_2) + \Phi(O_2)\frac{\min(z_{lim}, z_{mix})}{z_{mix}} - E(O_2) - F_v(O_2) \quad (5)$$

The inventory changes were calculated as the difference between two transects of the integrated $c(O_2)$ in the top 45 m. A constant integration depth of 45 m was chosen to capture the deepest extent of the deep chlorophyll maximum (z_{DCM}) found during the deployment, which likely represents the extent of the euphotic zone.

The inventory changes were calculated using the following equation:

$$I(O_2) = \frac{\int_0^{45\,m} C_{n+1}(z)dz - \int_0^{45\,m} C_n(z)dz}{t_{n+1} - t_n} \quad (6)$$

where n is the transect number, t is the day of the year and $C(z)$ is the vertical $c(O_2)$ profile. $I(O_2)$ is defined as the changes of the integrated $c(O_2)$ to z_{lim} in the same latitude bin between two dives.

The air-sea flux of oxygen, $\Phi(O_2)$ was calculated for each glider dive using the median $c(O_2)$, θ and S in the top 10 m. We followed the method of Woolf and Thorpe (1991) that includes the effect of bubble equilibrium supersaturation in the calculations:

$$\Phi(O_2) = k_w(O_2)\ \{(c(O_2) - [1 + \Delta_{bub}(O_2)]c_{sat}(O_2)\} \quad (7)$$

where $k_w(O_2)$ is the gas transfer coefficient, $\Delta_{bub}(O_2)$ is the increase of equilibrium saturation due to bubble injection and $c_{sat}(O_2)$ is the oxygen saturation. $c_{sat}(O_2)$ was calculated from S and θ using the solubility coefficients of Benson and Krause Jr (1984), as fitted by Garcia and Gordon (1992). $\Delta_{bub}(O_2)$ was calculated from the following equation:

$$\Delta_{bub}(O_2) = 0.01 \left(\frac{U}{U_0}\right)^2 \quad (8)$$

where U is 10 m-wind speed with 1 hour resolution (ECMWF ERA5, https://www.ecmwf.int/en/forecasts/datasets/reanalysis-datasets/era5) and U_0 represents the wind speed when the oxygen concentration is 1 % supersaturated and has a value of 9 m s^{-1} (Woolf and Thorpe, 1991). U has a spatial resolution of 0.25° latitude and 0.25° longitude and was interpolated to the glider position at the beginning of the dive.

The transfer velocity $k_w(O_2)$ was calculated based on Wanninkhof (2014):

$$\frac{k_w(O_2)}{\text{cm h}^{-1}} = 0.251 \left(\frac{Sc(O_2)}{660}\right)^{-0.5} \left(\frac{U}{\text{m s}^{-1}}\right)^2 \quad (9)$$

The Schmidt number, $Sc(O_2)$, was calculated using the parameterisation of Wanninkhof (2014). To account for wind speed variability, $k_w(O_2)$ applied to calculate $N(O_2)$ was a weighted mean based on the varying daily-mean wind speed U in the time interval between t_n and t_{n+1} (Δt) used to calculate $\frac{\Delta I(O_2)}{\Delta t}$ using a 5 points median z_{mix} and for 50 days to calculate $\Phi(O_2)$ (section 3.2) (Reuer et al., 2007).

The entrainment flux, $E(O_2)$, was calculated as the oxygen flux when the mixed layer depth deepens in time and is greater than z_{lim} at time t_2:

$$E(O_2) = \frac{I(O_2, t_1, z_{mix}(t_2))\frac{z_{lim}}{z_{mix(t_2)}} - I(O_2, t_1, z_{lim})}{t_2 - t_1} \quad (10)$$

where $t_2 - t_1$ represents the change in time, z_{mix} is the mixed layer depth, $I(O_2,t_1,z_{mix}(t_2))$, is the expected inventory that would result from a mixed layer deepening to $z_{mix}(t_2)$ between t_2 and t_1, and $I(O_2,t_1,z_{lim})$ is the original inventory at t_1.

The effect of diapycnal eddy diffusion (F_v) was calculated at z_{mix} when it was deeper than z_{lim} and at z_{lim} when z_{mix} was shallower than z_{lim}, using the following equation:

$$F_v(O_2) = K_z \frac{\partial c(O_2)}{\partial z} \quad (11)$$

for a vertical eddy diffusivity (K_z) of 10^{-5} m s^{-2} (Naveira Garabato et al., 2004). The effect of $F_v(O_2)$ on $N(O_2)$ was negligible (Figure A2b) with a median of (-0.06±0.34) mmol m^{-2} d^{-1}.

2.9 Calculation of dissolved inorganic carbon-based net community production, $N(C_T)$

$N(C_T)$ was expressed in mmol m^{-2} d^{-1} and was calculated from the C_T inventory changes $I(C_T)$, air-sea flux of CO_2, $\Phi(CO_2)$, entrainment $E(C_T)$ and diapycnal diffusion $F_v(C_T)$:

$$N(C_T) = -I(C_T) - \Phi(CO_2)\frac{\min(z_{lim},z_{mix})}{z_{mix}} + E(C_T) + F_v(C_T) \quad (12)$$

Firstly, $\Phi(CO_2)$ was calculated using the 10 m wind speed with 1 hour resolution downloaded from ECMWF ERA5. As for oxygen, we selected the closest wind speed data point at the beginning of each glider dive. We used the monthly mean atmospheric CO_2 dry mole fraction ($x(CO_2)$) downloaded from the Greenhouse Gases Reference Network Site (https://www.esrl.noaa.gov/gmd/ccgg/ggrn.php) closest to the deployment at Mace Head, County Galway, Ireland (Dlugokencky et al., 2015). Using $x(CO_2)$ we calculated the air-saturation concentration $c_{atm}(CO_2)$:

$$c_{atm}(CO_2) = x(CO_2)\, p_{baro}\, F(CO_2) \quad (13)$$

where p_{baro} is the mean sea level pressure and $F(CO_2)$ is the CO_2 solubility function calculated from surface θ and S (Weiss and Price, 1980).

The seawater $c(CO_2)$ at the surface was calculated using the median in the top 10 meters between the glider ascent and descent of the following dive $c(CO_2)$. From this, $\Phi(CO_2)$ was calculated:

$$\Phi(CO_2) = k(CO_2)\,[c(CO_2) - c_{atm}(CO_2)]. \quad (14)$$

$k(CO_2)$ was calculated using the parameterisation of Wanninkhof (2014):

$$\frac{k(CO_2)}{\text{cm h}^{-1}} = 0.251\left(\frac{Sc(CO_2)}{660}\right)^{-0.5}\left(\frac{U}{\text{m s}^{-1}}\right)^2 \quad (15)$$

363 $Sc(CO_2)$ is the dimensionless Schmidt number at the seawater temperature (Wanninkhof, 2014). To account for
364 wind speed variability, $k_w(CO_2)$ applied to calculate $N(O_2)$ was a weighted mean based on the varying daily-
365 mean wind speed U in the time interval between t_n and t_{n+1} (Δt) used to calculate $\frac{\Delta I(C_T)}{\Delta t}$ and for 50 days to
366 calculate $\Phi(CO_2)$ (section 3.2) (Reuer et al., 2007).

367 The inventory changes were calculated in the top 45 m with the following equation:

368 $$\frac{\Delta I(C)}{\Delta t} = \frac{\int_0^{45\ m} C_{n+1}\,dz - \int_0^{45\ m} C_n\,dz}{t_{n+1} - t_n} \quad (16)$$

369 The entrainment flux, $E(C_T)$ was calculated as the oxygen flux when the mixed layer depth deepens in time and
370 is greater than z_{lim} at time t_2:

371 $$E(C_T) = \frac{I(C,t_1,z_{mix}(t_2))\frac{z_{lim}}{z_{mix(t_2)}} - I(C,t_1,z_{lim})}{t_2 - t_1} \quad (17)$$

372 As for oxygen, the effect of diapycnal eddy diffusion (F_v) was calculated at z_{mix} when it was deeper than z_{lim} and
373 at z_{lim} when z_{mix} was shallower than z_{lim}, using the following equation:

374 $$F_v(C_T) = K_z \frac{\partial c(C_T)}{\partial z} \quad (18)$$

375 for a K_z of 10^{-5} m s^{-2} (Naveira Garabato et al., 2004). The effect of $F_v(C_T)$ was negligible (Figure A2a) with a
376 median of (0.07±0.3) mmol m^{-2} d^{-1}.

377 The contribution of horizontal advection to $N(C_T)$ was considered minimal over the timescales we calculated
378 inventory changes because previous studies have shown that changes in C_T during summer are mainly controlled
379 by biology and air-sea interactions (Gislefoss et al., 1998). For that reason, previous studies that estimated N in
380 the Norwegian Sea have also neglected advective fluxes (Falck and Anderson, 2005; Falck and Gade, 1999;
381 Kivimäe, 2007; Skjelvan et al., 2001).

382 Uncertainties in $N(C_T)$ and $N(O_2)$ were evaluated with a Monte-Carlo approach. The uncertainties of the input
383 variables are shown in Table 2; we repeated the analysis 1000 times. The total uncertainty in N was calculated as
384 the standard deviation of the 1000 Monte-Carlo simulations.

385

386

387

388 **Table 2.** Uncertainty associated with $N(C_T)$ and $N(O_2)$ input variables calculated by a Monte Carlo approach

Variable	Error	Reference/Method
C_T	10 µmol kg^{-1}	Standard deviation vs the water samples.
S	0.01	Standard deviation of glider salinities for $\sigma_0 > 1028$ kg m^{-3} and latitude > 64° N
θ	0.3 °C	Standard deviation of glider temperature for $\sigma_0 > 1028$ kg m^{-3} and latitude > 64° N
$c_{atm}(CO_2)$	1.5 µmol kg^{-1}	Standard deviation of $c_{atm}(CO_2)$
$c(CO_2)$	1.3 µmol kg^{-1}	Error is the standard deviation vs water samples.
$k(CO_2)$	20 %	(Wanninkhof, 2014)
z_{mix}	9 m	Standard deviation compared with z_{mix} based on thresholds ΔT = 0.1 °C (Sprintall and Roemmich, 1999), 0.2 °C (Thompson, 1976) and 0.8 °C (Kara et al., 2000).
$c(O_2)$	2.4 µmol kg^{-1}	Standard deviation of glider oxygen concentrations for $\sigma_0 > 1028$ kg m^{-3} and latitude > 64° N

389
390

391 **3 Results**

392 The uncorrected temperature θ, salinity S, $c(O_2)$, $p(CO_2)$ and c_{raw}(Chl *a*) presented in Figure 8 were analysed up
393 to dive 400 (24 July 2014). For the following dives, the CO_2 optode stopped sampling in the first 150 m (Figure
394 8d). The raw optode $c(O_2)$ data was calibrated and drift-corrected and $c(CO_2)$ was drift-, lag-corrected and
395 recalibrated, then used to quantify the temporal and spatial changes in N and Φ together with the quenching
396 corrected c_{raw}(Chl *a*) to evaluate net community production changes.

397

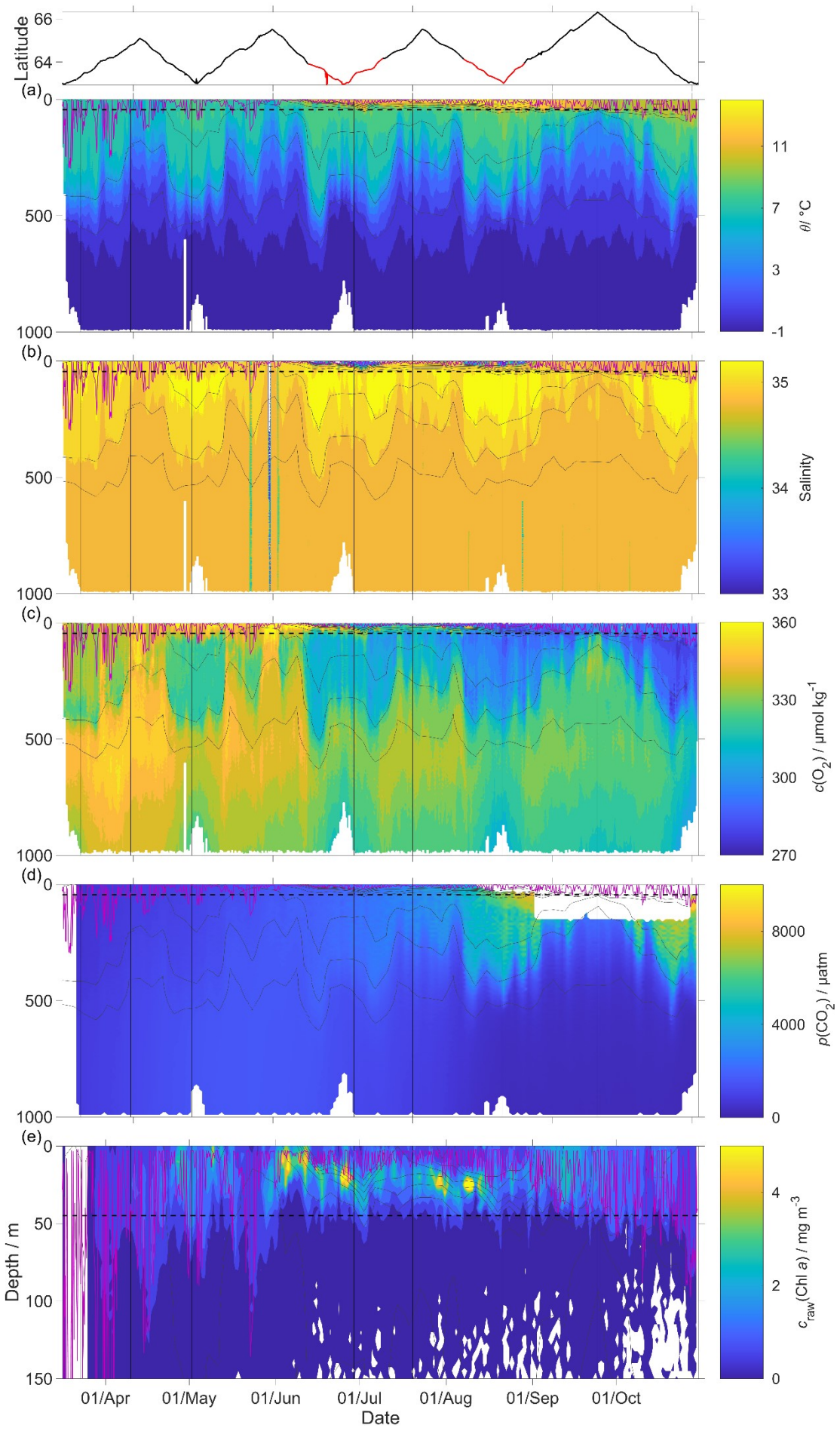
Latitude
66
64
(a)
0
500
1000
11
7
3
-1
θ/ °C
(b)
35
34
33
Salinity
(c)
360
330
300
270
c(O2) / µmol kg-1
(d)
8000
4000
0
p(CO2) / µatm
(e)
Depth / m
50
100
150
4
2
0
craw(Chl a) / mg m-3
01/Apr
01/May
01/Jun
01/Jul
01/Aug
01/Sep
01/Oct
Date

398

Figure 8: Raw glider data for all 703 dives with latitude of the glider trajectory at the top (black: NwAC; red: NCC, separated by a S of 35). a) temperature θ, b) salinity S, c) oxygen concentration $c(O_2)$, d) uncorrected CO_2 optode output $p_u(CO_2)$ and e) chlorophyll a concentration c_{raw}(Chl a). The white space means that the sensors did not measure any data. The pink line is z_{mix} calculated using a threshold criterion of $\Delta\theta = 0.5$ °C to a median θ of the top 5 m of the glider profile (Obata et al., 1996; United States. National Environmental Satellite and Information Service, Monterey and Levitus, 1997; Fo*ltz* et al., 2003), the black dotted line z_{lim} used as depth limit to calculate the net community production (N) and black contour lines are the isopycnals.

3.1 O_2 and CO_2 optode calibration

The uncorrected $c(O_2)$ continually decreased (Figure 8c). The ratio $c_C(O_2)/c_G(O_2)$ against day of the year used for the drift correction had a good correlation with time ($R^2 = 0.90$), showing a continuous increase of 0.0004 d^{-1} (Figure 3), equivalent to a decrease in the measured glider O_2 concentration of 0.11 µmol kg^{-1} d^{-1}. It was possible to apply the correction because $c_C(O_2)$ had low temporal variability for the chosen potential density σ_0 >1028 kg m^{-3}. The $c_C(O_2)$ values from OWSM and GLODAPv2 had a mean of (304.6±3.1) µmol kg^{-1}, varying from 294 to 315 µmol kg^{-1} (Figure A1). The drift correction reduced the variability of $c_G(O_2)$ in the selected potential density range from a standard deviation of 7.3 µmol kg^{-1} to a standard deviation of 2.4 µmol kg^{-1} (Figure 9).

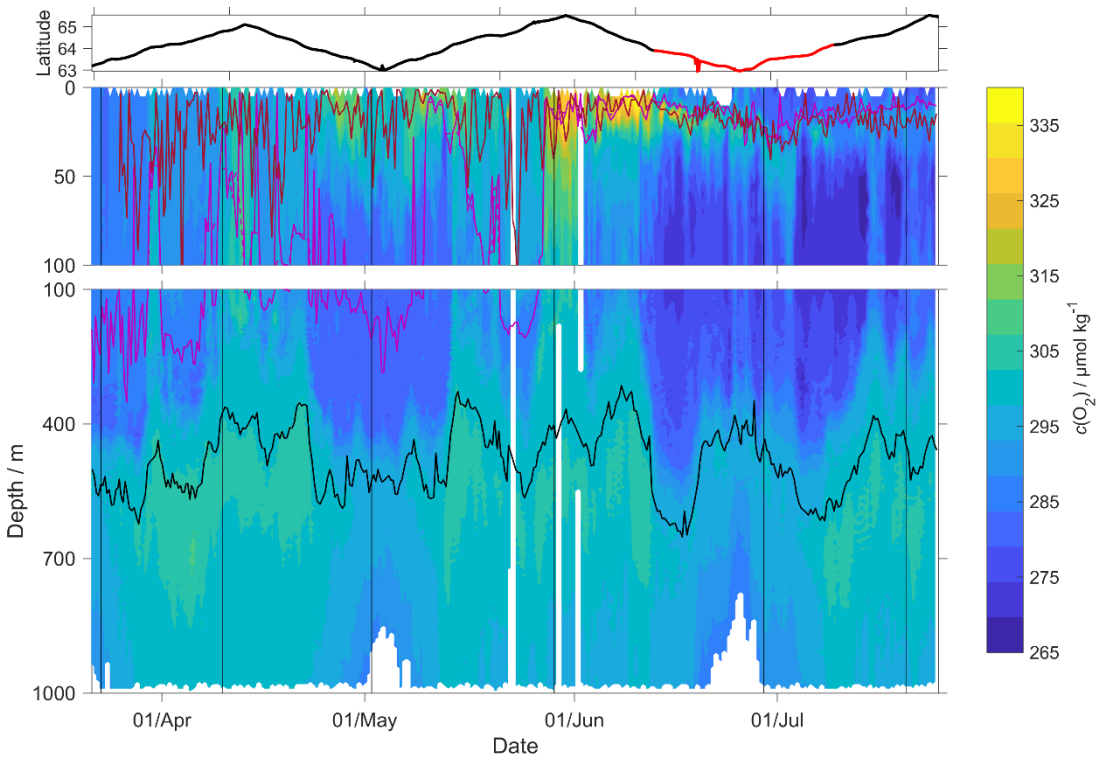

Figure 9: $c(O_2)$ contour plot with z_{DCM} (red line) and the z_{mix} (pink line) and z_{mix} using 5 points median (pink dotted line) calculated using a threshold criterion of $\Delta\theta = 0.5$ °C to median θ of the top 5 m of the glider profile (Obata et al., 1996; United States. National Environmental Satellite and Information Service, Monterey and Levitus, 1997; Fo*ltz* et al., 2003), in black $\sigma_0 = 1028$ kg m^{-3} and at the top the latitude trajectory of the glider in black NwAC and in red NCC.

Following drift, lag and scale corrections, glider fugacity $f_G(CO_2)$ derived from Eq. 2 had a mean difference of (8±22) µatm to the discrete samples (n = 55; not shown) and C_T had a standard deviation of 10 µmol kg^{-1} and a mean difference of 1.5 µmol kg^{-1} (Figure 10). $p(CO_2)$ and $f(CO_2)$ are almost identical, but $f(CO_2)$ takes into account of the non-ideal nature of the gas phase. The optode was able to capture the temporal and spatial variability showing that NCC had a lower concentration of C_T than NwAC. Restricting the $f(CO_2)$ comparison to the discrete samples *in* the top 10 m gave a mean difference of (21±21) µatm (n = 8). We also compared glider $f_G(CO_2)$ with SOCAT $f(CO_2)$ (Bakker et al., 2016) data in the region during the deployment (Figure 11). Until the beginning of June, there was general agreement between $f_G(CO_2)$ and $f_{SOCAT}(CO_2)$. Afterwards, $f_G(CO_2)$ varied between 326 and 434 µatm while $f_{SOCAT}(CO_2)$ varied between 259 and 354 µatm (Figure 11).

Our results are in agreement with Jeansson et al. (2011) who found the surface NCC was the region with the lowest C_T values (2083 µmol kg^{-1}) in the Norwegian Sea. This was confirmed during our deployment because C_T was (2100±18) µmol kg^{-1} in the NCC region and (2150±23) µmol kg^{-1} in the NwAC region (Figure 10) and $c(O_2)$ was > 300 µmol kg^{-1} in the NwAC and < 280 µmol kg^{-1} in the NCC.

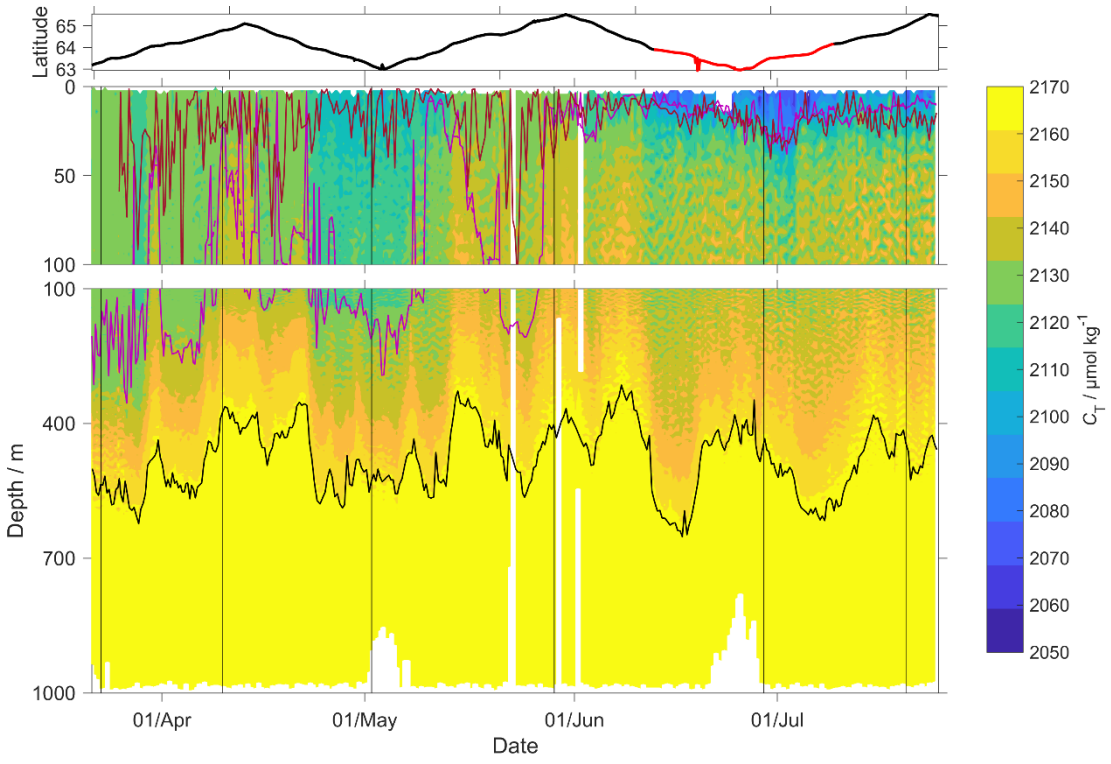

Figure 10: C_T contour plot with z_{DCM} (red line) and the z_{mix} (pink line) and z_{mix} using 5 points median (pink dotted line) calculated using a threshold criterion of $\Delta\theta$ = 0.5 °C to median θ of the top 5 m of the glider profile (Obata et al., 1996; United States. National Environmental Satellite and Information Service, Monterey and Levitus, 1997; Fo*ltz* et al., 2003), in black σ_0 = 1028 kg m^{-3} and at the top the latitude trajectory of the glider in black NwAC and in red NCC.

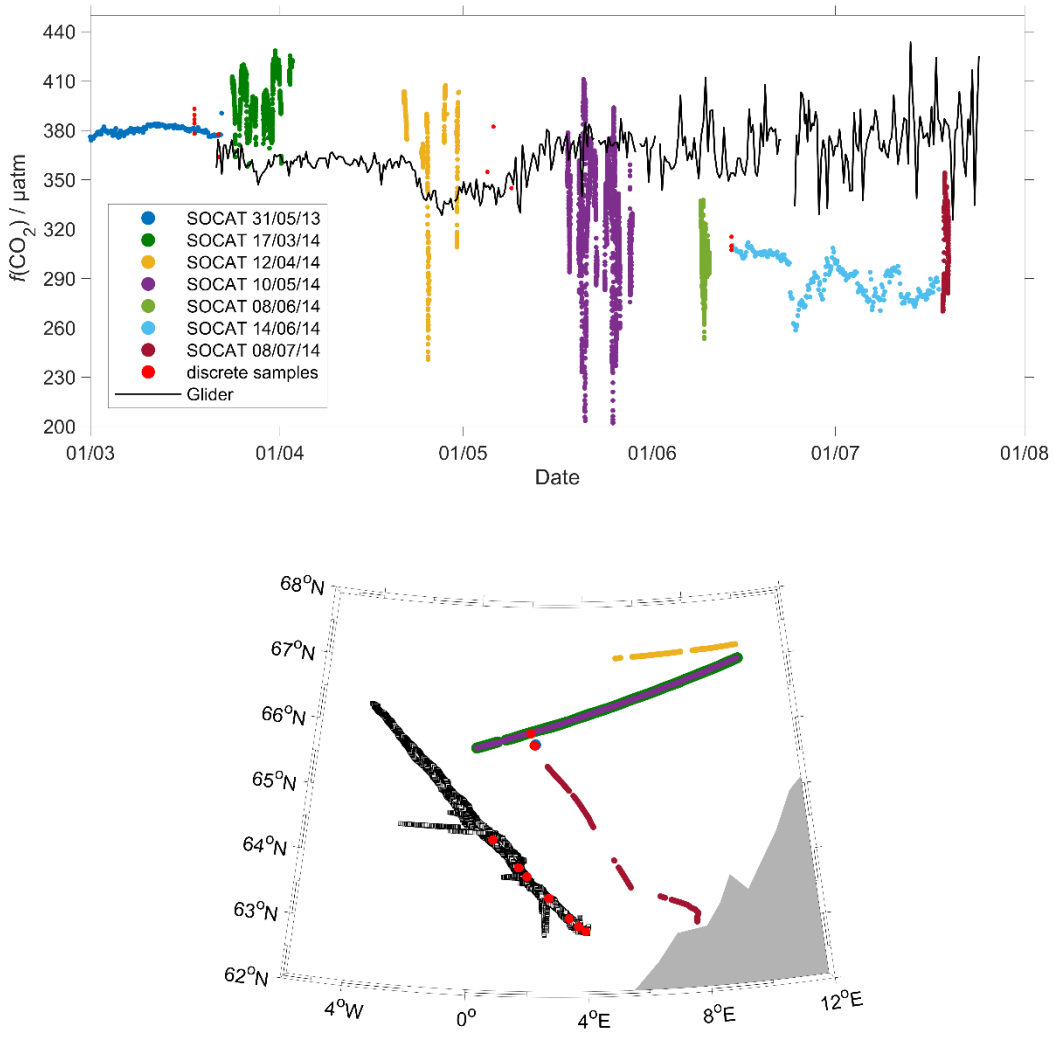

Figure 11: The plot represents the surface $f(CO_2)$ from 2014 SOCAT and from the glider. The black dots are the median of the glider $f(CO_2)$ in the top 10 meters calculated using the ascent of the single dive and the descent of the next dive. The red dots are the water samples collected during the deployment and the remaining dots are from the SOCAT cruises in the area during the deployment. On the bottom there is the map of the glider and SOCAT data positions.

3.2 Air-sea exchange

The surface water was supersaturated with oxygen all summer (Figure 12). From May this supersaturation drove a continuous O_2 flux from the sea to the atmosphere. However, the flux varied throughout the deployment having a median of 44 mmol m^{-2} d^{-1} (5^{th} centile: -16 mmol m^{-2} d^{-1}; 95^{th} centile: 103 mmol m^{-2} d^{-1}). Prior to the spring period of increased Chl *a* inventory, the supersaturation varied between 0 to 10 µmol kg^{-1}. $\Phi(O_2)$ had a median of -1.4 mmol m^{-2} d^{-1} (5^{th} centile: -49 mmol m^{-2} d^{-1}; 95^{th} centile: 23 mmol m^{-2} d^{-1}). Then, during the spring period of increased Chl *a* inventory, the surface concentration increased by over 35 µmol kg^{-1}, causing a peak in $\Phi(O_2)$ of 140 mmol m^{-2} d^{-1}. A second period of increased Chl *a* inventory was encountered in June and had a larger

463 $\Phi(O_2)$ up to 118 mmol m^{-2} d^{-1}, driven by supersaturation of 68 µmol kg^{-1}. The fluxes were smaller than during
464 the first period of increased Chl *a* and were associated by an increase of c_{raw}(Chl a) from 2.5 mg m^{-3} to the
465 summer maximum of 4.0 mg m^{-3}. However, prior to the spring period of increased Chl *a* inventory, $\Phi(O_2)$
466 showed a few days of influx into seawater caused by a decrease of θ from 7.6 °C to 5.9 °C that increased $c_{sat}(O_2)$.
467 The influx at the beginning of the deployment is partly due to the $\Delta_{bub}(O_2)$ correction that increased [1+
468 $\Delta_{bub}(O_2)]c_{sat}(O_2)$ to values larger than $c(O_2)$ for $U > 10$ m s^{-1}.

469 The CO_2 flux from March to July was always from the air to the sea (Figure 12), with a median of -3.9 mmol m^{-2}
470 d^{-1} (5^{th} centile: -11 mmol m^{-2} d^{-1}; 95^{th} centile: 0.3 mmol m^{-2} d^{-1}). An opposite flux direction is expected for $\Phi(O_2)$
471 and $\Phi(CO_2)$ during the productive season when net community production is the main driver of concentration
472 changes. After the summer period of increased Chl *a* inventory, the flux had a median of -1.1 mmol m^{-2} d^{-1} (5^{th}
473 centile: –5.1 mmol m^{-2} d^{-1}; 95^{th} centile: 1.7 mmol m^{-2} d^{-1}), in agreement with previous studies that classified the
474 Norwegian Sea as a CO_2 sink (Skjelvan et al., 2005; Takahashi et al., 2002). $\Phi(CO_2)$ for the discrete samples
475 from 18 March to 14 June (n = 13) varied from 0.1 to -13 mmol m^{-2} d^{-1}.

476
477
478
479
480
481
482

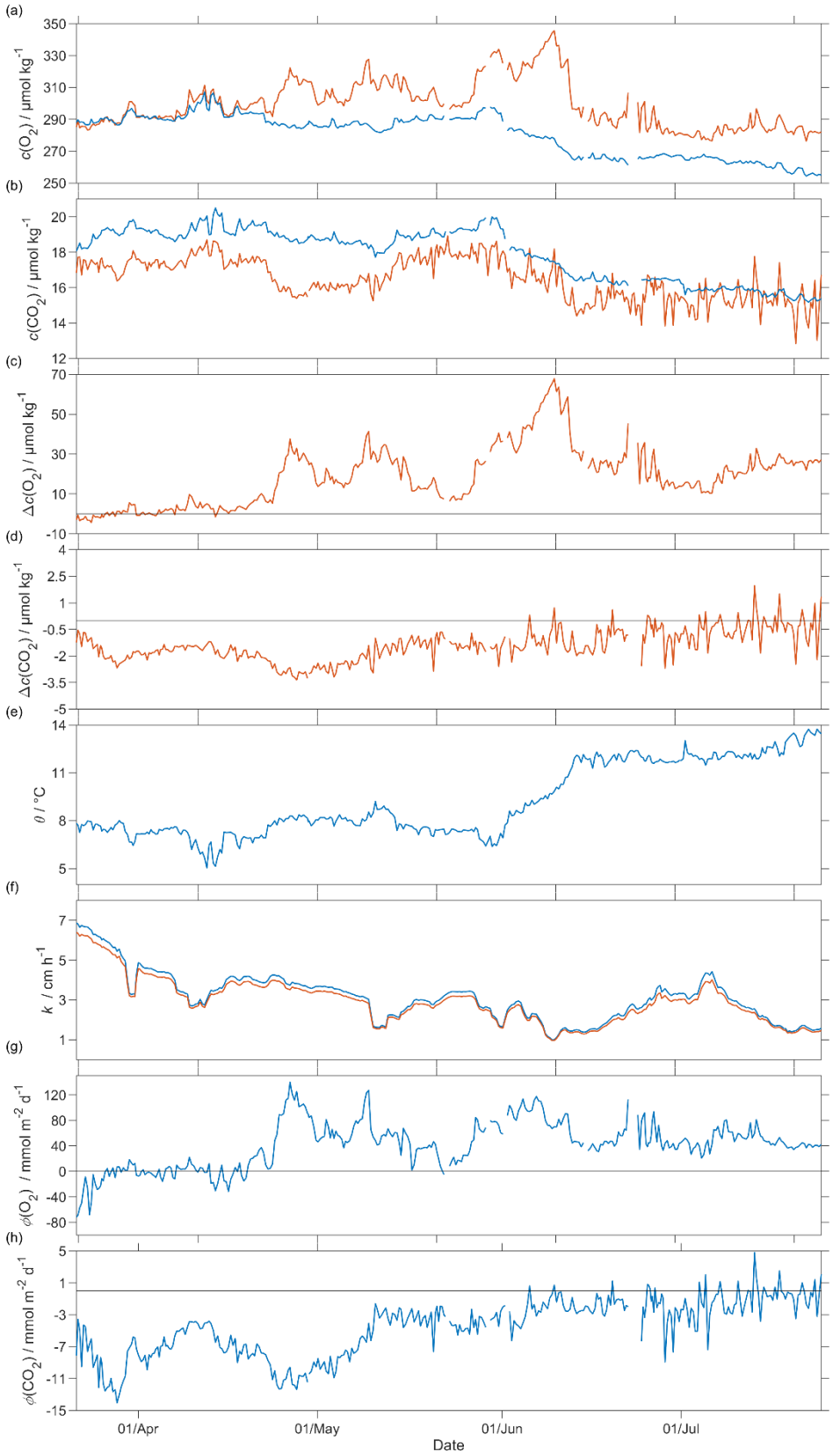

Figure 12: Oxygen and CO_2 air-sea flux where a) shows in blue $c_{sat}(O_2)$ and in red $c(O_2)$, b) shows in blue $c_{sat}(CO_2)$ and in red $c(CO_2)$, c) $\Delta c(O_2) = c(O_2) - c_{sat}(O_2)$, d) $\Delta c(CO_2) = c(CO_2) - c_{sat}(CO_2)$, e) sea surface temperature θ, f) $k_w(O_2)$ (blue) and $k(CO_2)$ normalised back to 50 days (Reuer et al., 2007), g) oxygen air-sea

flux $\Phi(O_2)$ and h) CO_2 air-sea flux $\Phi(CO_2)$. The flux from sea to air is positive while that from air to sea is negative.

3.3 $N(O_2)$

We calculated $N(O_2)$ and $N(C_T)$ using an integration depth of z_{lim} = 45 m because the mean deep chlorophyll maximum (DCM) depth was z_{DCM} = (20±18 m) (Figure 9). For comparison, the mixed layer depth was deeper and varied more strongly and had a mean value of z_{mix} = (68±78) m, using a threshold criterion of $\Delta\theta$ = 0.5 °C to the median θ value of the top 5 m of the glider profile (Obata et al., 1996; United States. National Environmental Satellite and Information Service, Monterey and Levitus, 1997; Foltz et al., 2003). Using a 5 points moving median maintained the same mean value of z_{mix} but decreased the variability = (68±75) m.

The two N values were calculated as the difference in inventory changes between two transects when the glider moved in the same direction. This method was used in order to have similar time interval between repeat occupations of the same transect position to calculate the inventory changes and entrainment.

During the deployment, we sampled two periods of increased Chl a inventory, the first one in May and a second one in June. The chlorophyll a inventory ($I_{\mathrm{raw},z_{\mathrm{lim}}}(\mathrm{Chl}\ a)$) was calculated integrating c_{raw}(Chl a) to z_{lim}. The fluorometer was not calibrated for that reason to remove any outliers we used a five-point moving mean of $I_{\mathrm{raw},z_{\mathrm{lim}}}(\mathrm{Chl}\ a)$.

The changes of $N(O_2)$ were dominated by $\Phi(O_2)$ that had an absolute median of 47 mmol m^{-2} d^{-1} (5^{th} centile: 4.1 mmol m^{-2} d^{-1}; 95^{th} centile: 103 mmol m^{-2} d^{-1}), followed by $I(O_2)$ that had a median of 12 mmol m^{-2} d^{-1} (5^{th} centile: 2.8 mmol m^{-2} d^{-1}; 95^{th} centile: 20 mmol m^{-2} d^{-1}), $F_v(O_2)$ that had an absolute median of 0.2 mmol m^{-2} d^{-1} (5^{th} centile: 0 mmol m^{-2} d^{-1}; 95^{th} centile: 0.9 mmol m^{-2} d^{-1}) and $E(O_2)$ that had a median of 0 mmol m^{-2} d^{-1} (5^{th} centile: 0 mmol m^{-2} d^{-1}; 95^{th} centile: 0.4 mmol m^{-2} d^{-1}).

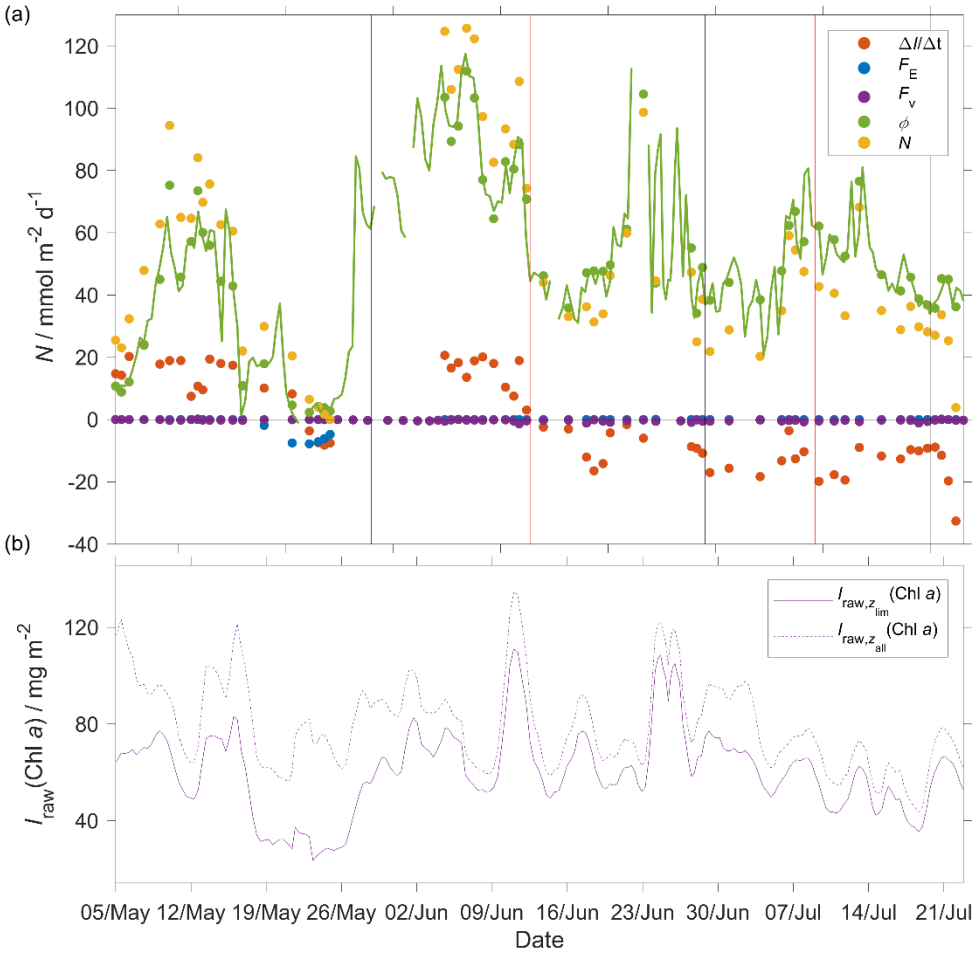

Figure 13: a) Each component of the $N(O_2)$ calculation: in red $I(O_2)$, $E(O_2)$ in blue, in violet $F_v(O_2)$, $\Phi(O_2)$ in green dots and the green line is $\Phi(O_2)$ continuous timeseries calculated using $k_w(O_2)$ weighted 50 days and in yellow $N(O_2) = I(O_2) + \Phi(O_2)\frac{\min(z_{lim},z_{mix})}{z_{mix}} - E(O_2) - F_v(O_2)$ b) the violet continuous line is the c_{raw}(Chl a) inventory in the top 45 m, z_{lim}, ($I_{raw,z_{lim}}$(Chl a)) and the dotted line in all the water columun, z_{all}, ($I_{raw,z_{all}}$(Chl a)). The black vertical lines represent each glider transect and between the two vertical red lines when the glider was in NCC.

During the summer $I_{raw,z_{lim}}$(Chl a) increased to 110 mg m^{-2}, which caused a sharp increase of $N(O_2)$ to (126±25) mmol m^{-2} d^{-1}. $I_{raw,z_{lim}}$(Chl a) remained higher than 50 mg m^{-2} until the end of June when $N(O_2)$ was (31±9) mmol m^{-2} d^{-1}. The passage of the glider from NwAC to NCC accompanied by a drop of surface $c(O_2)$ from 330 to 280 µmol kg^{-1} (Figure 9) that resulted in lower $\Phi(O_2)$ and $N(O_2)$ values (Figure 13). At the same time $I_{raw,z_{lim}}$(Chl a) decreased to 35 mg m^{-2} showing that the decrease of $N(O_2)$ depended on the passage to NCC and a decrease of biological production.

At the beginning of May, $I_{raw,z_{lim}}$(Chl a) increased to 97 mg m^{-2} and $N(O_2)$ = (94±16) mmol m^{-2} d^{-1}. After this period, $I_{raw,z_{lim}}$(Chl a) decreased to 49 mg m^{-2} and $N(O_2)$ = (0±1.6) mmol m^{-2} d^{-1}.

Using the mean of $N(O_2)$ assuming an $N(O_2) = 0$ in the rest of the year lead to an annual value of 4 mol m^{-2} a^{-1} (Table 3) discussed in section 4.2.

Table 3. *N* estimates in the Norwegian Sea. The previous studies dataset had data collected by several cruises in different years, Falck and Anderson (2005) used historical data from 1960 to 2000 collected all the year in the area from 62 to 70° N and from 1991 to 1994 collected at OWSM. Skjelvan et al., (2001) used data collected all the year from 67.5° N 9° E to 71.5° N 1° E and along 74.5° N from 7 to 15° E from 1957 to 1970 and from 1991 to 1998. Kivimäe (2007) used the oxygen measured at OWSM all the year from 1955 to 2005 and Falck and Gade (1999) used data collected all the year in all the Norwegian Sea from 1955 to 1988.

Study	$N(C_T)$ / mol m^{-2} a^{-1}	$N(O_2)$ / mol m^{-2} a^{-1}	z_{lim} / m	Variables used to derive *N*
(Falck and Anderson, 2005)	3.4	—	100	$c(NO_3^-)$, $c(PO_4^{3-})$, C_T
(Skjelvan et al., 2001)	2.0	2.6	300	$c(O_2)$, $c(PO_4^{3-})$
(Kivimäe, 2007)	8.6	11	z_{mix} until 100 m	$c(O_2)$
(Falck and Gade, 1999)	3.0	3.9	30	$c(O_2)$
This study	1.0	4.0	30	$c(O_2)$, C_T
This study	0.9	4.0	45	$c(O_2)$, C_T
This study	0.4	3.7	100	$c(O_2)$, C_T

3.4 *N*(C_T)

In the case of $N(C_T)$ the main driver were the inventory changes with an absolute median of 7.6 mmol m^{-2} d^{-1} (5th centile: 1 mmol m^{-2} d^{-1}; 95th centile: 23 mmol m^{-2} d^{-1}), followed by $\Phi(CO_2)$ that had an absolute median of 1.7 mmol m^{-2} d^{-1} (5th centile: 0.3 mmol m^{-2} d^{-1}; 95th centile: 4 mmol m^{-2} d^{-1}), $F_v(C_T)$ that had an absolute median of 0.2 mmol m^{-2} d^{-1} (5th centile: 0 mmol m^{-2} d^{-1}; 95th centile: 0.7 mmol m^{-2} d^{-1}) and $E(C_T)$ had a median of 0 mmol m^{-2} d^{-1} (5th centile: 0 mmol m^{-2} d^{-1}; 95th centile: 3.3 mmol m^{-2} d^{-1}). During the period of increased Chl *a* inventory $N(C_T)$ was (23±4.2) mmol m^{-2} d^{-1}. Later $I_{\mathrm{raw},z_{\mathrm{lim}}}(\mathrm{Chl}\ a)$ decreased to 30 mg m^{-2} driving $N(C_T)$ to negative values with a minimum of (-4.5±5.2) mmol m^{-2} d^{-1}. In the next transect, the glider measured the maximum $I_{\mathrm{raw},z_{\mathrm{lim}}}(\mathrm{Chl}\ a)$ of 111 mg m^{-2} that increased $N(C_T)$ to (14±8.7) mmol m^{-2} d^{-1}. In the next transect the glider moved in NCC that had a C_T of 2075 µmol kg^{-1} at the surface compared with the 2130 µmol kg^{-1} in NwAC and drove a continuous positive $N(C_T)$ that had a maximum of (26±3.7) mmol m^{-2} d^{-1} (Figure 14).

Using the mean of $N(C_T)$ with the assumption that during the rest of year $N(C_T) = 0$, we calculated the annual $N(C_T)$ of 0.9 mol m^{-2} a^{-1} (Table 3) that its implications are discussed in section 4.2.

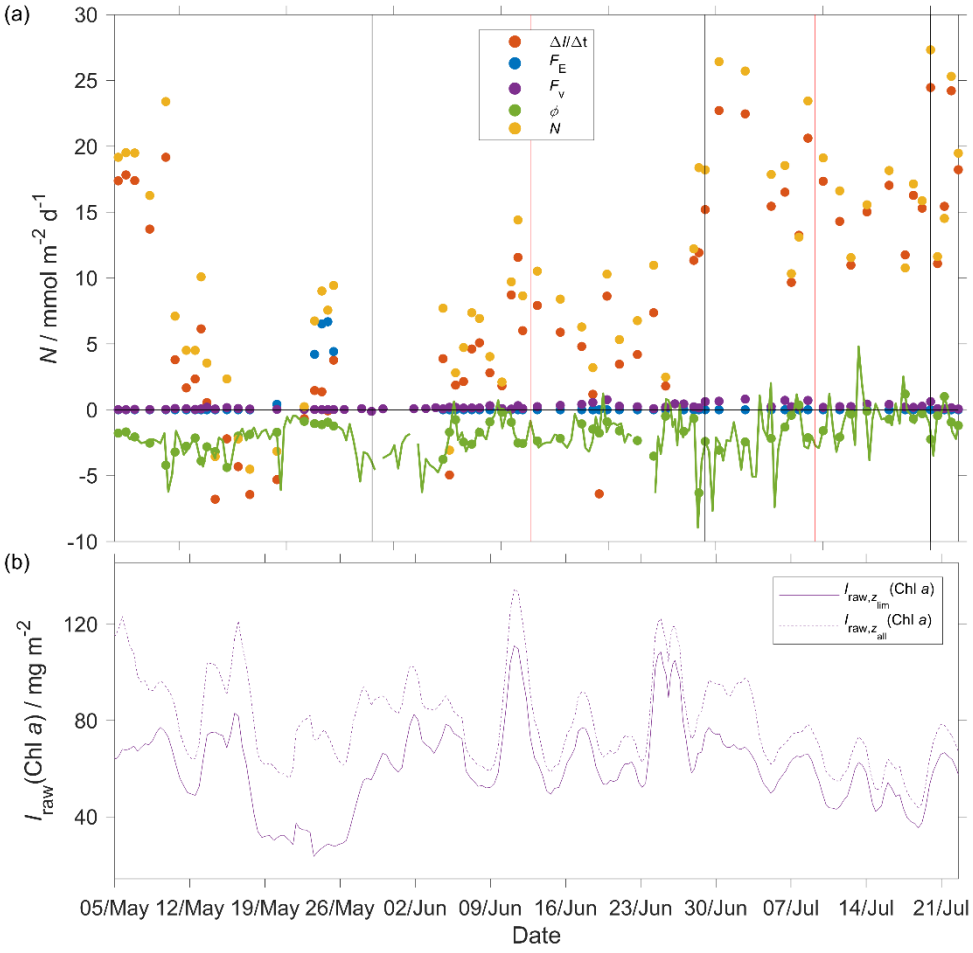

Figure 14: a) Each component of the $N(C_T)$ calculation: in red $I(C_T)$, $E(C_T)$ in blue, $F_v(C_T)$ in violet, $\Phi(C_T)$ in green dots and the green line is $\Phi(O_2)$ continuous time-series calculated using $k(CO_2)$ weighted 50 days and in yellow $N(C_T) = -I(C_T) - \Phi(CO_2)\frac{\min(z_{lim}, z_{mix})}{z_{mix}} + E(C_T) + F_v(C_T)$ b) the violet continuous line is the c_{raw}(Chl a) inventory in the top 45 m, z_{lim}, ($I_{raw,z_{lim}}$(Chl a)) and the dotted line in all the water columun, z_{all}, ($I_{raw,z_{all}}$(Chl a)). The black vertical lines represent each glider transect and between the two vertical red lines when the glider was in NCC.

4 Discussion

4.1 Sensor performance

This study presents data from the first glider deployment with a CO_2 optode. The initial uncalibrated $p(CO_2)$, $p_U(CO_2)$, measured by the CO_2 optode had a median of 604 µatm (5th centile: 566 µatm; 95th centile: 768 µatm when the $p(CO_2)$ of discrete samples varied from 302 to 421 µatm. This discrepancy was caused by sensor drift prior to and during deployment of the optode.

We applied corrections for drift (using deep-water samples as a reference point), sensor lag and calibrated the CO_2 optode against co-located discrete samples throughout the water column.

Atamanchuk (2014) reported that the sensor was affected by a lag that varied from 45 to 264 s depending on temperature. These values were determined in an actively stirred beaker. However, in this study the sensor was mounted on a glider and was not actively pumped, which increased the response time to (1384 s, 25th quartile: 1101 s; 75th quartile: 1799 s). Also, the optode was affected by a continuous drift from 637 to 5500 µatm that is larger than the drift found by Atamanchuk et al. (2015a) that increased by 75 µatm after 7 months.

In this study, the drift- and lag-corrected sensor output showed a better correlation with the CO_2 concentration $c(CO_2)$ than with $p(CO_2)$. The latter two quantities are related to each other by the solubility that varies with θ and S (Weiss, 1974) (Eq. 2). The better correlation with $c(CO_2)$ was probably related due to an inadequate temperature-parameterisation of the sensor calibration function. The sensor output depends on the changes in pH that are directly related to the changes of $c(CO_2)$ in the membrane and – indirectly – $p(CO_2)$, via Henry's Law. The calibration is supposed to correct for the temperature-dependence of the sensor output (Atamanchu*k et al*, 2014). So the fact, that the sensor output correlated better with $c(CO_2)$ than $p(CO_2)$ is perhaps due to a fortuitous cancellation of an inadequate temperature-parameterisation and the Henry's Law relationship between $c(CO_2)$ than $p(CO_2)$.

The calibrated optode output captured the C_T changes in space and time with a standard deviation of 10 µmol kg^{-1} compared with the discrete samples. C_T decreased from 2100 µmol kg^{-1} to 2050 µmol kg^{-1} and increased with depth to 2170 µmol kg^{-1}. This shows the potential of the sensor for future studies that aim to analyse the carbon cycle using a high-resolution dataset.

The optode-derived CO_2 fugacity $f_G(CO_2)$ had a mean bias of (8±22) µatm compared with the discrete samples. These values are comparable with a previous study when the CO_2 optode was tested for 65 days on a wave-powered Profiling crAWLER (PRAWLER) from 3 to 80 m (Chu et al., 2020), which had an uncertainty between 35 and 72 µatm. The PRAWLER optode was affected by a continuous drift of 5.5 µatm d^{-1} corrected using a regional empirical algorithm that uses $c(O_2)$, θ, S and σ_o to estimate A_T and C_T.

4.2 Norwegian Sea net community production

Increases in $N(O_2)$ and $N(C_T)$ were associated with increases in depth-integrated c_{raw}(Chl a), designated as periods of increased Chl *a* inventory, at the beginning of May and in June. During the first period of increased Chl *a* inventory at the beginning of May surface c_{raw}(Chl *a*) reached 3 mg m^{-3}. The second period of increased Chl *a* inventory in June lasted longer and c_{raw}(Chl *a*) increased to 4 mg m^{-3}. Between the two periods of increased Chl *a* inventory $N(C_T)$ had negative values and $N(O_2)$ reached the deployment minimum indicating that remineralisation of the high Chl *a* inventory material was a dominant process during this period. Even though

599 they are uncalibrated, the spring period of increased Chl *a* inventory c_{raw}(Chl *a*) values are in agreement with the
600 study of Rey (2001) who found c_{raw}(Chl *a*) = 3 mg m^{-3} at the beginning of May. The largest period of increased
601 Chl *a* inventory when the top 50 m θ increased from 7 °C to 11 °C and z_{mix} shoaled from 200 m to 20 m. During
602 this period, $c(O_2)$ reached a summer maximum of 340 µmol kg^{-1} and C_T decreased to the summer minimum at
603 2070 µmol kg^{-1}. In both cases, the main components of the *N* changes were the inventory and air-sea flux, while
604 the smallest driver was the entrainment. Also, the glider sampled two different water masses characterised by
605 different C_T and $c(O_2)$. This led to smaller values of $N(O_2)$ and higher values $N(C_T)$ in NCC compared with
606 NwAC (Figure 13 and 14).

607 Table 3 shows estimates of net community production (*N*) in the Norwegian Sea (Falck and Anderson, 2005;
608 Falck and Gade, 1999; Kivimäe, 2007; Skjelvan et al., 2001). All these studies used low-resolution datasets in
609 space and time. These datasets had data collected by several cruises in different years, Falck and Anderson
610 (2005) used historical data from 1960 to 2000 collected in the area from 62 to 70° N and from 1991 to 1994
611 collected all the year at OWSM. Skjelvan et al., (2001) used data collected from 67.5° N 9° E to 71.5° N 1° E
612 and along 74.5° N from 7 to 15° E from 1957 to 1970 and from 1991 to 1998. Kivimäe (2007) used the oxygen
613 measured all the year at OWSM from 1955 to 2005 and Falck and Gade (1999) used data collected all the year in
614 all the Norwegian Sea from 1955 to 1988. The estimated *N* in the 4 studies varies from 2.0 to 8.6 mol m^{-2} a^{-1} for
615 $N(C_T)$ and from 2.6 to 11.1 mol m^{-2} a^{-1} for $N(O_2)$. In our study, we obtained an annual $N(C_T)$ of 0.9 mol m^{-2} a^{-1}
616 and a $N(O_2)$ of 4 mol m^{-2} a^{-1} in agreement with these studies. The larger $N(O_2)$ compared with $N(C_T)$ should be
617 attributed to the large $\Phi(O_2)$ that had an absolute median of 47 mmol m^{-2} d^{-1} compared with $\Phi(CO_2)$ absolute
618 median of 1.7 mmol m^{-2} d^{-1}. Instead, the inventory changes were similar between $N(O_2)$ and $N(C_T)$ with a median
619 of 12 mmol m^{-2} d^{-1} and 7.6 mmol m^{-2} d^{-1}, respectively. To compare our results with previous studies we used the
620 same z_{lim} of 30 m(Falck and Gade, 1999) and 100 m (Falck and Anderson, 2005; Kivimäe, 2007). The calculated
621 $N(C_T; 30\ m)$ was 1 mol m^{-2} a^{-1}, $N(C_T; 100\ m)$ was 0.4 mol m^{-2} a^{-1}, $N(O_2; 30\ m)$ was 4 mol m^{-2} a^{-1} and $N(O_2; 100$
622 m) was 3.7 mol m^{-2} a^{-1}. In the case of $N(C_T; 30\ m)$ and $N(C_T; 100\ m)$ the values calculated were smaller to the
623 previous studies where $N(C_T)$ varied from 2 to 8.6 mol m^{-2} a^{-1}. The smallest value was for $N(C_T; 100\ m)$ because
624 it included the not productive layer located under the euphotic zone and the z_{mix} where the remineralisation of the
625 organic matter can increase C_T. The calculated $N(O_2)$ was not affected by the selection of z_{lim} because the
626 changes were largely controlled by $\Phi(O_2)$. However, the calculated $N(O_2)$ was in agreement with the previous
627 studies where varied from 2.6 to 11 mol m^{-2} a^{-1}.

628 Some of the previous $N(C_T)$ estimates derived C_T from other variables such as $c(O_2)$, $c(PO_4^{3-})$, $c(NO_3^-)$,
629 assuming Redfield ratios P:C:O$_2$ 1:106-138 (Redfield, 1963). Our $N(C_T)$ estimate was 0.5 mol m^{-2} a^{-1} and is

lower to 3.4 mol m^{-2} a^{-1} estimated by Falck and Anderson (2005) who used C_T samples directly. The difference between our $N(C_T)$ and other studies is likely due to their use of the Redfield ratio assumption (Redfield, 1963) to convert $N(O_2)$ to $N(C_T)$. The carbon/nutrients ratios vary between water masses and during photosynthesis (Copin-Montégut, 2000; Körtzinger et al., 2001; Osterroht and Thomas, 2000; Thomas et al., 1999). In deep waters, the release ratios vary for C_T, $c(PO_4^{3-})$, $c(NO_3^-)$ and $c(O_2)$ leading to different concentrations than the traditional Redfield ratio (Hupe and Karstensen, 2000; Minster and Boulahdid, 1987; Shaffer, 1996). For example, during remineralisation, NO_3^- and PO_4^{3-} are released faster than C_T leading to a C:P remineralisation ratio of 90 ± 15 at the base of the euphotic zone to about 125 ± 10 from to 1000 m to the bottom (Shaffer, 1996).

The difference of $N(O_2)$ and $N(C_T)$ is caused by the yearly variability of N in the Norwegian Sea. In fact, Kivimäe (2007) saw an annual variability of $N(O_2)$ from 1955 to 2005 of 4.7 mol m^{-2} a^{-1} to 18.3 mol m^{-2} a^{-1} and of $N(C_T)$ of 3.6 mol m^{-2} a^{-1} to 14.0 mol m^{-2} a^{-1}. In order to understand what is causing these interannual changes, it is important to use available high-resolution datasets. Also, this study showed that the Norwegian Sea spring and summer N is strongly affected by time and location. For that reason, N estimated from low-resolution datasets make the result strongly dependant on the time and place of sampling. To quantify this interannual variability in N, more high-resolution studies are needed.

5 Conclusions

This study was, to the best of our knowledge, the first glider deployment of a CO_2 optode. During the deployment, the optode performance was affected by drift, lag, lack of sampling in the top 150 m after dive 400 (the 24 July 2014), and poor default calibration. We found that the optode response was better correlated with $c(CO_2)$ than $p(CO_2)$. Nevertheless, the optode was able to capture the spatial and temporal changes in the Norwegian Sea after recalibration with discrete samples collected along the glider section and nearby at OWSM during the deployment.

C_T estimated from glider data had a standard deviation of 10 µmol kg^{-1} and a mean bias of 1.5 µmol kg^{-1} compared with the discrete samples, while the CO_2 fugacity $f(CO_2)$ had a mean bias of (8±23) µatm. The dataset was used to calculate net community production $N(O_2)$ and $N(C_T)$ from inventory changes, air-sea flux, and entrainment. The two N values had maxima during the summer period of increased Chl *a* inventory of $N(C_T)$ = (14±8.7) mmol m^{-2} d^{-1} and $N(O_2)$ = (126±25) mmol m^{-2} d^{-1}. At the beginning of April, we sampled a smaller spring period of increased Chl *a* inventory with a $N(C_T)$ = (23±4.2) mmol m^{-2} d^{-1} and $N(O_2)$ = (94±24) mmol m^{-2} d^{-1}. After the period of increased Chl *a* inventory, $N(C_T)$ decreased due to remineralisation to (-4.5±5.2) mmol m^{-2} d^{-1}, and $N(O_2)$ to (0±1.5) mmol m^{-2} d^{-1}. The glider monitored two water masses (NwAC and NCC). The NCC-

influenced one was characterised by a lower $c(O_2)$ and C_T than the NwAC region. $N(O_2)$ decreased to (3.9±7.3) mmol m^{-2} d^{-1} driven by a decrease of $c(O_2)$ under 30 m from 300 to 290 µmol kg^{-1} and increased for $N(C_T)$ to (26±3.7) mmol m^{-2} d^{-1}. In particular, the $N(O_2)$ changes were driven by the surface oxygen supersaturation making the seawater a source of oxygen. In contrast, the ocean was a sink of inorganic carbon during the summer, with a continuous CO_2 flux from the atmosphere into the water.

This deployment shows the potential of using small, low energy consuming CO_2 optodes on autonomous observing platforms like Seagliders to quantify the interactions between biogeochemical processes and the marine carbonate system at high spatiotemporal resolution.

Data availability. The glide data are available on Norwegian Marine Data Centre (NMDC) at https://doi.org/10.21335/NMDC-1654657723

Competing interests. The author declares that there is no conflict of interest.

Acknowledgements. Luca Possenti's PhD project is part of The Next Generation Unmanned Systems Science (NEXUSS) Centre for Doctoral Training which is funded by the Natural Environment Research Council (NERC) and the Engineering and Physical Science Research Council (EPSRC) [grant number NE/N012070/1]. We would like to thank the scientists, engineers, and crew that contributed to the glider mission and data collection, as well as Michael Hemming and Bastien Queste for their initial contributions to the data analysis.

6 References

Alkire, M. B., Lee, C., D'Asaro, E., Perry, M. J., Briggs, N., Cetinić, I. and Gray, A.: Net community production and export from Seaglider measurements in the North Atlantic after the spring bloom, J. Geophys. Res. Ocean., 119(9), 6121–6139, 2014.

Atamanchuk, D.: Development and use of an optical pCO2 sensor in marine studies, 2013.

Atamanchuk, D., Tengberg, A., Thomas, P. J., Hovdenes, J., Apostolidis, A., Huber, C. and Hall, P. O. J.: Performance of a lifetime-based optode for measuring partial pressure of carbon dioxide in natural waters, Limnol. Oceanogr. Methods, 12(2), 63–73, doi:10.4319/lom.2014.12.63, 2014.

Atamanchuk, D., Kononets, M., Thomas, P. J., Hovdenes, J., Tengberg, A. and Hall, P. O. J.: Continuous long-term observations of the carbonate system dynamics in the water column of a temperate fjord, J. Mar. Syst., 148, 272–284, doi:10.1016/j.jmarsys.2015.03.002, 2015a.

Atamanchuk, D., Tengberg, A., Aleynik, D., Fietzek, P., Shitashima, K., Lichtschlag, A., Hall, P. O. J. and Stahl, H.: Detection of CO2 leakage from a simulated sub-seabed storage site using three different types of pCO2 sensors, Int. J. Greenh. Gas Control, 38, 121–134, doi:10.1016/j.ijggc.2014.10.021, 2015b.

Bakker, D. C. E., Pfeil, B., Landa, C. S., Metzl, N., Brien, K. M. O., Olsen, A., Smith, K., Cosca, C., Harasawa, S. and Jones, S. D.: A multi-decade record of high-quality f CO 2 data in version 3 of the Surface Ocean CO 2 Atlas (SOCAT), , 383–413, doi:10.5194/essd-8-383-2016, 2016.

Benson, B. B. and Krause Jr, D.: The concentration and isotopic fractionation of oxygen dissolved in freshwater and seawater in equilibrium with the atmosphere 1, Limnol. Oceanogr., 29(3), 620–632, 1984.

Binetti, U., Kaiser, J., Damerell, G. M., Rumyantseva, A., Martin, A. P., Henson, S. and Heywood, K. J.: Net community oxygen production derived from Seaglider deployments at the Porcupine Abyssal Plain site (PAP; northeast Atlantic) in 2012–13, Prog. Oceanogr., 183, 102293, 2020.

Bittig, H. C.: Tackling Oxygen Optode Drift : Near-Surface and In-Air Oxygen Optode Measurements on a Float Provide an Accurate in Situ Reference, , (November), 1536–1543, doi:10.1175/JTECH-D-14-00162.1, 2015.

Bittig, H. C., Fiedler, B., Steinhoff, T. and Körtzinger, A.: OCEANOGRAPHY : METHODS A novel electrochemical calibration setup for oxygen sensors and its use for the stability assessment of Aanderaa optodes, , 1, 921–933, doi:10.4319/lom.2012.10.921, 2012.

von Bültzingslöwen, C., McEvoy, A. K., McDonagh, C., MacCraith, B. D., Klimant, I., Krause, C. and Wolfbeis, O. S.: Sol–gel based optical carbon dioxide sensor employing dual luminophore referencing for application in food packaging technology, Analyst, 127(11), 1478–1483, 2002.
Bushinsky, S. M., Takeshita, Y. and Williams, N. L.: Observing Changes in Ocean Carbonate Chemistry: Our Autonomous Future, Curr. Clim. Chang. reports, 5(3), 207–220, 2019.
Chu, S. N., Sutton, A. J., Alin, S. R., Lawrence-Slavas, N., Atamanchuk, D., Mickett, J. B., Newton, J. A., Meinig, C., Stalin, S. and Tengberg, A.: Field evaluation of a low-powered, profiling p CO2 system in coastal Washington, Limnol. Oceanogr. Methods, n.d.
Copin-Montégut, C.: Consumption and production on scales of a few days of inorganic carbon, nitrate and oxygen by the planktonic community: results of continuous measurements at the Dyfamed Station in the northwestern Mediterranean Sea (May 1995), Deep Sea Res. Part I Oceanogr. Res. Pap., 47(3), 447–477, 2000.
Degrandpre, M. D.: Measurement of Seawater pC02 Using a Renewable-Reagent Fiber Optic Sensor with Colorimetric Detection, , 1172(8), 331–337, doi:10.1021/ac00052a005, 1993.
Dickson, A. G.: Thermodynamics of the dissociation of boric acid in synthetic seawater from 273 . 15 to 318 . 15 K, , 37(5), 755–766, 1990.
Dlugokencky, E. J., Lang, P. M., Masarie, K. A., Crotwell, A. M. and Crotwell, M. J.: Atmospheric carbon dioxide dry air mole fractions from the NOAA ESRL Carbon Cycle Cooperative Global Air Sampling Network, 1968–2014, NOAA ESRL Glob. Monit. Div. Boulder, CO, USA, 2015.
Ducklow, H. W. and Doney, S. C.: What Is the Metabolic State of the Oligotrophic Ocean ? A Debate, , doi:10.1146/annurev-marine-121211-172331, 2013.
Falck, E. and Anderson, L. G.: The dynamics of the carbon cycle in the surface water of the Norwegian Sea, , 94, 43–53, doi:10.1016/j.marchem.2004.08.009, 2005.
Falck, E. and Gade, G.: Net community production and oxygen fluxes in the Nordic Seas based on O2 budget calculations, , 13(4), 1117–1126, 1999.
Fiedler, B., Fietzek, P., Vieira, N., Silva, P., Bittig, H. C. and Körtzinger, A.: In situ CO2 and O2 measurements on a profiling float, J. Atmos. Ocean. Technol., 30(1), 112–126, doi:10.1175/JTECH-D-12-00043.1, 2013.
Foltz, G. R., Grodsky, S. A., Carton, J. A. and McPhaden, M. J.: Seasonal mixed layer heat budget of the tropical Atlantic Ocean, J. Geophys. Res. Ocean., 108(C5), 2003.
Friedlingstein, P., Jones, M., O'Sullivan, M., Andrew, R., Hauck, J., Peters, G., Peters, W., Pongratz, J., Sitch, S. and Le Quéré, C.: Global carbon budget 2019, Earth Syst. Sci. Data, 11(4), 1783–1838, 2019.
Garcia, H. E. and Gordon, L. I.: Oxygen solubility in seawater: Better fitting equations, Limnol. Oceanogr., 37(6), 1307–1312, 1992.
Gattuso, J.-P. and Hansson, L.: Ocean acidification, Oxford University Press., 2011.
Gislefoss, J. S., Nydal, R., Slagstad, D., Sonninen, E. and Holme, K.: Carbon time series in the Norwegian sea, , 45, 433–460, 1998.
Gourcuff, C.: ANFOG Slocum CTD data correction, , (March), 2014.
Goyet, C., Walt, D. R. and Brewer, P. G.: Development of a fiber optic sensor for measurement of pCO2 in sea water: design criteria and sea trials, Deep Sea Res. Part A. Oceanogr. Res. Pap., 39(6), 1015–1026, 1992.
Hagebo, M. and Rey, F.: Storage of seawater for nutrients analysis, Fisk. Hav., 4, 1, 12, 1984.
Hansen, B. and Østerhus, S.: North Atlantic – Nordic Seas exchanges, , 45, 109–208, 2000.
Hardman-Mountford, N. J., Moore, G., Bakker, D. C. E., Watson, A. J., Schuster, U., Barciela, R., Hines, A., Moncoiffé, G., Brown, J., Dye, S., Blackford, J., Somerfield, P. J., Holt, J., Hydes, D. J. and Aiken, J.: An operational monitoring system to provide indicators of CO 2-related variables in the ocean, ICES J. Mar. Sci., 65(8), 1498–1503, doi:10.1093/icesjms/fsn110, 2008.
Haskell, W. Z., Hammond, D. E., Prokopenko, M. G., Teel, E. N., Seegers, B. N., Ragan, M. A., Rollins, N. and Jones, B. H.: Net Community Production in a Productive Coastal Ocean From an Autonomous Buoyancy-Driven Glider, J. Geophys. Res. Ocean., 124(6), 4188–4207, 2019.
Hemsley, J. M.: OBSERVATIONS PLATFORMS| Buoys, 2015.
Hemsley, V. S., Smyth, T. J., Martin, A. P., Frajka-williams, E., Thompson, A. F., Damerell, G. and Painter, S. C.: Estimating Oceanic Primary Production Using Vertical Irradiance and Chlorophyll Pro fi les from Ocean Gliders in the North Atlantic, , doi:10.1021/acs.est.5b00608, 2015.
Van Heuven, S., Pierrot, D., Rae, J. W. B., Lewis, E. and Wallace, D. W. R.: MATLAB program developed for CO2 system calculations, ORNL/CDIAC-105b. Carbon Dioxide Inf. Anal. Center, Oak Ridge Natl. Lab. US Dep. Energy, Oak Ridge, Tennessee, 530, 2011.
Hupe, A. and Karstensen, J.: Redfield stoichiometry in Arabian Sea subsurface waters, Global Biogeochem. Cycles, 14(1), 357–372, 2000.
Jeansson, E., Olsen, A., Eldevik, T., Skjelvan, I., Omar, A. M., Lauvset, S. K., Nilsen, J. E. Ø., Bellerby, R. G. J., Johannessen, T. and Falck, E.: The Nordic Seas carbon budget : Sources , sinks , and uncertainties, , 25(2002), 1–16, doi:10.1029/2010GB003961, 2011.
Kara, A. B., Rochford, P. A. and Hurlburt, H. E.: An optimal definition for ocean mixed layer depth, J. Geophys. Res. Ocean., 105(C7), 16803–16821, 2000.
Kivimäe, C.: Carbon and oxygen fluxes in the Barents and Norwegian Seas: production, air-sea exchange and

765 budget calculations, 2007.
766 Klimant, I., Huber, C., Liebsch, G., Neurauter, G., Stangelmayer, A. and Wolfbeis, O. S.: Dual lifetime
767 referencing (DLR)—a new scheme for converting fluorescence intensity into a frequency-domain or time-
768 domain information, in New Trends in Fluorescence Spectroscopy, pp. 257–274, Springer., 2001.
769 Körtzinger, A., Thomas, H., Schneider, B., Gronau, N., Mintrop, L. and Duinker, J. C.: At-sea intercomparison
770 of two newly designed underway pCO2 systems—encouraging results, Mar. Chem., 52(2), 133–145, 1996.
771 Körtzinger, A., Koeve, W., Kähler, P. and Mintrop, L.: C: N ratios in the mixed layer during the productive
772 season in the northeast Atlantic Ocean, Deep Sea Res. Part I Oceanogr. Res. Pap., 48(3), 661–688, 2001.
773 Lee, K., Tong, L. T., Millero, F. J., Sabine, C. L., Dickson, A. G., Goyet, C., Park, G. H., Wanninkhof, R., Feely,
774 R. A. and Key, R. M.: Global relationships of total alkalinity with salinity and temperature in surface waters of
775 the world's oceans, Geophys. Res. Lett., 33(19), 1–5, doi:10.1029/2006GL027207, 2006.
776 Lee, K., Kim, T., Byrne, R. H., Millero, F. J., Feely, R. A. and Liu, Y.: The universal ratio of boron to chlorinity
777 for the North Pacific and North Atlantic oceans, Geochim. Cosmochim. Acta, 74(6), 1801–1811,
778 doi:10.1016/j.gca.2009.12.027, 2010.
779 Lockwood, D., Quay, P. D., Kavanaugh, M. T., Juranek, L. W., Feely, R. A. and À, Æ. C. À.: High-resolution
780 estimates of net community production and air-sea CO 2 flux in the northeast Pacific, , 26, 1–16,
781 doi:10.1029/2012GB004380, 2012.
782 Lueker, T. J., Dickson, A. G. and Keeling, C. D.: Ocean pCO2 calculated from DIC, TA, and the Mehrbach
783 equations for K1 and K2: Validation using laboratory measurements of CO2 in gas and seawater at equilibrium,
784 Abstr. Pap. Am. Chem. Soc., 217, U848–U848, 2000.
785 Martz, T. R., Connery, J. G. and Johnson, K. S.: Testing the Honeywell Durafet for seawater pH applications,
786 Limnol. Oceanogr. Methods, 8, 172–184, doi:10.4319/lom.2010.8.172, 2010.
787 Medeot, N., Nair, R. and Gerin, R.: Laboratory Evaluation and Control of Slocum Glider C – T Sensors, , 838–
788 846, doi:10.1175/2011JTECHO767.1, 2011.
789 Miloshevich, L.: Development and Validation of a Time-Lag Correction for Vaisala Radiosonde Humidity
790 Measurements, , 1305–1328, 2004.
791 Minster, J.-F. and Boulahdid, M.: Redfield ratios along isopycnal surfaces—a complementary study, Deep Sea
792 Res. Part A. Oceanogr. Res. Pap., 34(12), 1981–2003, 1987.
793 Monteiro, P. M. S., Schuster, U., Hood, M., Lenton, A., Metzl, N., Olsen, A., Rogers, K., Sabine, C., Takahashi,
794 T. and Tilbrook, B.: A global sea surface carbon observing system: Assessment of changing sea surface CO2 and
795 air-sea CO2 fluxes, Proc. Ocean., 9, 702–714, 2009.
796 Naveira Garabato, A. C., Oliver, K. I. C., Watson, A. J. and Messias, M.: Turbulent diapycnal mixing in the
797 Nordic seas, J. Geophys. Res. Ocean., 109(C12), 2004.
798 Neftel, A., Oeschger, H., Schwander, J., Stauffer, B. and Zumbrunn, R.: Ice core sample measurements give
799 atmospheric CO 2 content during the past 40,000 yr, Nature, 295(5846), 220–223, 1982.
800 Neuer, S., Cianca, A., Helmke, P., Freudenthal, T., Davenport, R., Meggers, H. and Knoll, M.: Progress in
801 Oceanography Biogeochemistry and hydrography in the eastern subtropical North Atlantic gyre . Results from
802 the European time-series station ESTOC, , 72, 1–29, doi:10.1016/j.pocean.2006.08.001, 2007.
803 Nicholson, D., Emerson, S. and Eriksen, C. C.: Net community production in the deep euphotic zone of the
804 subtropical North Pacific gyre from glider surveys, Limnol. Oceanogr., 53(5 PART 2), 2226–2236,
805 doi:10.4319/lo.2008.53.5_part_2.2226, 2008.
806 Nicholson, D. P. and Feen, M. L.: Air calibration of an oxygen optode on an underwater glider, Limnol.
807 Oceanogr. Methods, 15(5), 495–502, doi:10.1002/lom3.10177, 2017.
808 Nilsen, J. E. Ø. and Falck, E.: Progress in Oceanography Variations of mixed layer properties in the Norwegian
809 Sea for the period 1948 – 1999, , 70, 58–90, doi:10.1016/j.pocean.2006.03.014, 2006.
810 Obata, A., Ishizaka, J. and Endoh, M.: Global verification of critical depth theory for phytoplankton bloom with
811 climatological in situ temperature and satellite ocean color data, J. Geophys. Res. Ocean., 101(C9), 20657–
812 20667, 1996.
813 Olsen, A., Key, R. M., Van Heuven, S., Lauvset, S. K., Velo, A., Lin, X., Schirnick, C., Kozyr, A., Tanhua, T.,
814 Hoppema, M., Jutterström, S., Steinfeldt, R., Jeansson, E., Ishii, M., Pérez, F. F. and Suzuki, T.: The global
815 ocean data analysis project version 2 (GLODAPv2) - An internally consistent data product for the world ocean,
816 Earth Syst. Sci. Data, 8(2), 297–323, doi:10.5194/essd-8-297-2016, 2016.
817 Osterroht, C. and Thomas, H.: New production enhanced by nutrient supply from non-Redfield remineralisation
818 of freshly produced organic material, J. Mar. Syst., 25(1), 33–46, 2000.
819 Pachauri, R. K. and Reisinger, A.: IPCC fourth assessment report, IPCC Fourth Assess. Rep., 1, 976 [online]
820 Available from:
821 http://www.construible.es/construible%5Cbiblioteca%5Cpresentacion_informe_ipcc.pdf%5Cnpapers2://publicat
822 ion/uuid/DD3ABB67-E411-4C0F-A29C-DA693B95B789, 2007.
823 Peeters, F., Atamanchuk, D., Tengberg, A., Encinas-Fernández, J. and Hofmann, H.: Lake metabolism:
824 Comparison of lake metabolic rates estimated from a diel CO2-and the common diel O2-technique, PLoS One,
825 11(12), 2016.
826 Plant, J. N., Johnson, K. S., Sakamoto, C. M., Jannasch, H. W., Coletti, L. J., Riser, S. C. and Swift, D. D.: Net

community production at Ocean Station Papa observed with nitrate and oxygen sensors on profiling floats, Global Biogeochem. Cycles, 30(6), 859–879, 2016.
Quay, P., Stutsman, J. and Steinhoff, T.: Primary production and carbon export rates across the subpolar N. Atlantic Ocean basin based on triple oxygen isotope and dissolved O2 and Ar gas measurements, Global Biogeochem. Cycles, 26(2), 2012.
Le Quéré, C., Raupach, M. R., Canadell, J. G., Marland et al., G., Le Quéré et al., C., Le Quéré et al., C., Raupach, M. R., Canadell, J. G., Marland, G., Bopp, L., Ciais, P., Conway, T. J., Doney, S. C., Feely, R. A., Foster, P., Friedlingstein, P., Gurney, K., Houghton, R. A., House, J. I., Huntingford, C., Levy, P. E., Lomas, M. R., Majkut, J., Metzl, N., Ometto, J. P., Peters, G. P., Prentice, I. C., Randerson, J. T., Running, S. W., Sarmiento, J. L., Schuster, U., Sitch, S., Takahashi, T., Viovy, N., van der Werf, G. R. and Woodward, F. I.: Trends in the sources and sinks of carbon dioxide, Nat. Geosci., 2(12), 831–836, doi:10.1038/ngeo689, 2009.
Redfield, A. C.: The influence of organisms on the composition of seawater, sea, 2, 26–77, 1963.
Rérolle, V. M. C., Floquet, C. F. A., Harris, A. J. K., Mowlem, M. C., Bellerby, R. R. G. J. and Achterberg, E. P.: Development of a colorimetric microfluidic pH sensor for autonomous seawater measurements, Anal. Chim. Acta, 786, 124–131, 2013.
Reuer, M. K., Barnett, B. A., Bender, M. L., Falkowski, P. G. and Hendricks, M. B.: New estimates of Southern Ocean biological production rates from O2/Ar ratios and the triple isotope composition of O2, Deep Sea Res. Part I Oceanogr. Res. Pap., 54(6), 951–974, 2007.
Rey, B. F.: 5 . Phytoplankton : the grass of the sea, , (cl), 2001.
Sabine, C. L., Feely, R. A., Gruber, N., Key, R. M., Lee, K., Bullister, J. L., Wanninkhof, R., Wong, C. S. S., Wallace, D. W. R., Tilbrook, B., Millero, F. J., Peng, T.-H. T.-H., Kozyr, A., Ono, T., Rios, A. F., A., F. R., Gruber, N., Key, R. M., Lee, K., Bullister, J. L., Wanninkhof, R., Wong, C. S. S., Wallace, D. W. R., Tilbrook, B., Millero, F. J., Peng, T.-H. T.-H., Kozyr, A., Ono, T. and Rios, A. F.: The oceanic sink for anthropogenic CO2, Science (80-.)., 305(5682), 367–371, doi:10.1126/science.1097403, 2004.
Saderne, V., Fietzek, P. and Herman, P. M. J.: Extreme Variations of pCO2 and pH in a Macrophyte Meadow of the Baltic Sea in Summer: Evidence of the Effect of Photosynthesis and Local Upwelling, PLoS One, 8(4), 2–9, doi:10.1371/journal.pone.0062689, 2013.
Saetre, R. and Ljoen, R.: THE NORWEGIAN COASTAL CURRENT, 1972.
Seguro, I., Marca, A. D., Painting, S. J., Shutler, J. D., Suggett, D. J. and Kaiser, J.: High-resolution net and gross biological production during a Celtic Sea spring bloom, Prog. Oceanogr., 177, 101885, 2019.
Seidel, M. P., Degrandpre, M. D. and Dickson, A. G.: A sensor for in situ indicator-based measurements of seawater pH, , 109, 18–28, doi:10.1016/j.marchem.2007.11.013, 2008.
Shaffer, G.: Biogeochemical cycling in the global ocean 2. New production, Redfield ratios, and remineralization in the organic pump, , 101, 3723–3745, 1996.
Sharples, J., Ross, O. N., Scott, B. E., Greenstreet, S. P. R. and Fraser, H.: Inter-annual variability in the timing of stratification and the spring bloom in the North-western North Sea, Cont. Shelf Res., 26(6), 733–751, 2006.
Skjelvan, I., Falck, E., Anderson, L. G. and Rey, F.: Oxygen fluxes in the Norwegian Atlantic Current, Mar. Chem., 73(3–4), 291–303, doi:10.1016/S0304-4203(00)00112-2, 2001.
Skjelvan, I., Anderson, L. G., Falck, E. and Anders, K.: A Review of the Inorganic Carbon Cycle of the Nordic Seas and Barents Sea and Christoph through the strength area of 15-75, 2005.
Skjelvan, I., Falck, E., Rey, F. and Kringstad, S. B.: Inorganic carbon time series at Ocean Weather Station M in the Norwegian Sea, , 549–560, 2008.
Sprintall, J. and Roemmich, D.: Characterizing the structure of the surface layer in the Pacific Ocean, J. Geophys. Res. Ocean., 104(C10), 23297–23311, 1999.
Sutton, A. J., Sabine, C. L., Meinig, C. and Feely, R. A.: A high-frequency atmospheric and seawater p CO 2 data set from 14 open-ocean sites using a moored autonomous system, , 353–366, doi:10.3334/CDIAC/OTG.TSM, 2014.
Swift, J. H.: The arctic waters, in The Nordic Seas, pp. 129–154, Springer., 1986.
Takahashi, T., Sutherland, S. C., Sweeney, C., Poisson, A., Metzl, N., Tilbrook, B., Bates, N., Wanninkhof, R., Feely, R. A., Sabine, C., Olafsson, J. and Nojiri, Y.: Global sea – air CO 2 flux based on climatological surface ocean p CO 2 , and seasonal biological and temperature effects, , 49, 1601–1622, 2002.
Takahashi, T., Sutherland, S. C., Wanninkhof, R., Sweeney, C., Feely, R. A., Chipman, D. W., Hales, B., Friederich, G., Chavez, F., Sabine, C., Watson, A., Bakker, D. C. E., Schuster, U., Yoshikawa-Inoue, H., Ishii, M., Midorikawa, T., Nojiri, Y., Körtzinger, A., Steinhoff, T., Hoppema, M., Olafsson, J., Arnarson, T. S., Johannessen, T., Olsen, A., Bellerby, R., Wong, C. S., Delille, B., Bates, N. R. and de Baar, H. J. W.: Climatological mean and decadal change in surface ocean pCO2, and net sea–air CO2 flux over the global oceans, Deep Sea Res. Part II Top. Stud. Oceanogr., 56(8), 554–577, doi:10.1016/j.dsr2.2008.12.009, 2009.
Tengberg, A., Hovdenes, J., Andersson, H. J., Brocandel, O., Diaz, R. and Hebert, D.: OCEANOGRAPHY : METHODS Evaluation of a lifetime-based optode to measure oxygen in aquatic systems, , (1964), 7–17, 2006.
Thomas, H., Ittekkot, V., Osterroht, C. and Schneider, B.: Preferential recycling of nutrients—the ocean's way to increase new production and to pass nutrient limitation?, Limnol. Oceanogr., 44(8), 1999–2004, 1999.
Thomas, P. J., Atamanchuk, D., Hovdenes, J. and Tengberg, A.: The use of novel optode sensor technologies for

monitoring dissolved carbon dioxide and ammonia concentrations under live haul conditions, Aquac. Eng., 77, 89–96, 2017.
Thompson, R. O. R. Y.: Climatological numerical models of the surface mixed layer of the ocean, J. Phys. Oceanogr., 6(4), 496–503, 1976.
United States. National Environmental Satellite and Information Service, D., Monterey, G. I. and Levitus, S.: Seasonal variability of mixed layer depth for the world ocean, US Department of Commerce, National Oceanic and Atmospheric Administration …., 1997.
Wanninkhof, R.: OCEANOGRAPHY : METHODS Relationship between wind speed and gas exchange over the ocean revisited, , 351–362, doi:10.4319/lom.2014.12.351, 2014.
Weiss, R. F.: Carbon dioxide in water and seawater: the solubility of a non-ideal gas, Mar. Chem., 2(3), 203–215, doi:10.1016/0304-4203(74)90015-2, 1974.
Weiss, R. F. and Price, B. A.: Nitrous oxide solubility in water and seawater, Mar. Chem., 8(4), 347–359, 1980.
Woolf, D. K. and Thorpe, S. A.: Bubbles and the air-sea exchange of gases in near-saturation conditions, J. Mar. Res., 49(3), 435–466, 1991.

7 Appendices

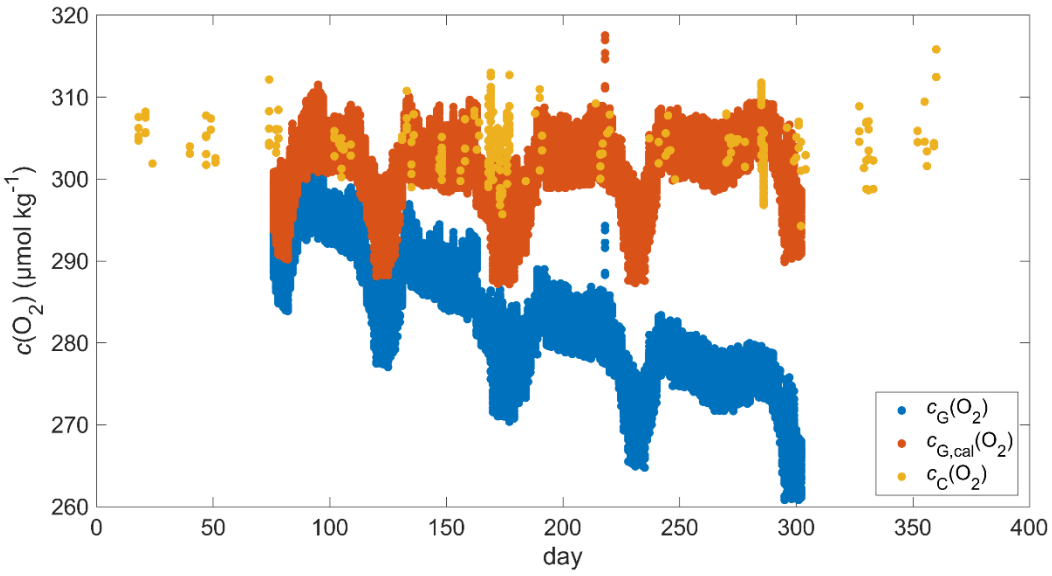

Figure A1: discrete samples $c_C(O_2)$ (yellow), raw glider oxygen $c_G(O_2)$ (blue) and drift corrected glider oxygen $c_{G,cal}(O_2)$ (red) for a potential density > 1028 kg m^{-3}.

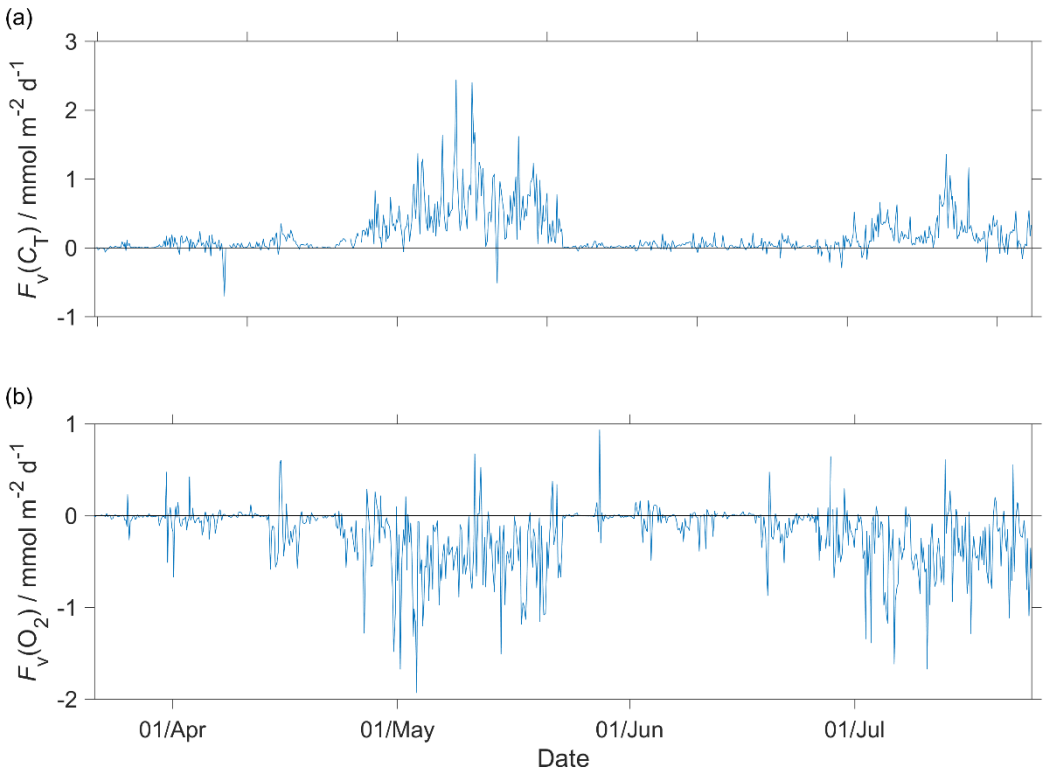

909

910 **Figure A2:** Diapycnal mixing (F_v) calculated for the glider descent and ascent for a) C_T and b) O_2 at the mixed
911 layer depth (z_{mix}) when deeper than 45 m (z_{lim}) and at z_{lim} when z_{mix} was shallower than 45 m. In the calculations
912 we used a vertical eddy diffusivity (K_z) of 10^{-5} m s^{-2} (Naveira Garabato et al., 2004).